Article

Microporous water with high gas solubilities

https://doi.org/10.1038/s41586-022-05029-w

Received: 19 September 2021

Accepted: 28 June 2022

Published online: 24 August 2022

Check for updates

Daniel P. Erdosy[1,7], Malia B. Wenny[1,7], Joy Cho[1,7], Christopher DelRe[1], Miranda V. Walter[1], Felipe Jiménez-Ángeles[2], Baofu Qiao[2], Ricardo Sanchez[1], Yifeng Peng[3,4], Brian D. Polizzotti[3,4], Monica Olvera de la Cruz[2,5,6] & Jarad A. Mason[1]✉

Liquids with permanent microporosity can absorb larger quantities of gas molecules than conventional solvents[1], providing new opportunities for liquid-phase gas storage, transport and reactivity. Current approaches to designing porous liquids rely on sterically bulky solvent molecules or surface ligands and, thus, are not amenable to many important solvents, including water[2–4]. Here we report a generalizable thermodynamic strategy to preserve permanent microporosity and impart high gas solubilities to liquid water. Specifically, we show how the external and internal surface chemistry of microporous zeolite and metal–organic framework (MOF) nanocrystals can be tailored to promote the formation of stable dispersions in water while maintaining dry networks of micropores that are accessible to gas molecules. As a result of their permanent microporosity, these aqueous fluids can concentrate gases, including oxygen (O_2) and carbon dioxide (CO_2), to much higher densities than are found in typical aqueous environments. When these fluids are oxygenated, record-high capacities of O_2 can be delivered to hypoxic red blood cells, highlighting one potential application of this new class of microporous liquids for physiological gas transport.

Water is the ubiquitous solvent for all biological processes and for many of the chemical transformations critical to sustainable energy generation, storage and utilization. Its polarity and propensity for hydrogen bonding promote the solvation of polar substances but inhibit the dissolution of non-polar substances, including most gases[5]. The low solubility of gases in water—often an order of magnitude lower than in common organic solvents—imposes fundamental limitations on many biomedical and energy-related technologies that require the transport of gas molecules through aqueous fluids. For instance, low densities of dissolved O_2 hinder tissue engineering and cell culture in vitro and make it challenging to treat various types of life-threatening hypoxia in vivo[6]. Aqueous-phase gas transport also limits the performance of fuel cells and the space-time yield and efficiency of many important electrocatalytic reactions—including CO_2 reduction, N_2 reduction and CH_4 oxidation[7,8].

Owing to their high internal surface areas and pore volumes, microporous solids can concentrate gas molecules through adsorption to far higher densities than can be dissolved in a typical liquid solvent—or that exist in a bulk gas phase—at a given temperature and pressure[9]. Recently, it has been shown that permanent microporosity is not exclusively a feature of solid-state materials and can be extended to the liquid phase in a nascent class of materials known as porous liquids[1]. All porous liquids developed so far consist of microporous nanocrystals or organic cage molecules dispersed in organic solvents or ionic liquids that are too large to diffuse through the pore entrances, leaving the micropores vacant and accessible to gas molecules[2–4]. Because of their intrinsic microporosity, these liquids can store much higher quantities of gas molecules than the corresponding non-porous liquid[10]. This sterics-based approach to preserving permanent microporosity within liquids is not, however, transferable to aqueous systems because a micropore that is large enough to adsorb nearly any gas molecule will also be large enough to accommodate H_2O molecules.

Certain proteins and molecular cavitands contain pores that are accessible to H_2O molecules but remain dry in aqueous solution owing to the presence of hydrophobic side chains or functional groups that impart a thermodynamic penalty for H_2O molecules residing within the non-polar pore instead of within the bulk liquid[11,12]. Taking inspiration from these systems, we pursued a new strategy to create liquids with permanent microporosity and high gas sorption capacities based on thermodynamics rather than sterics. Specifically, we proposed that microporous nanocrystals with hydrophobic internal surfaces and hydrophilic external surfaces could be designed to form uniform, stable dispersions in water, within which it is more thermodynamically favourable for water to interact with other water molecules in the bulk liquid phase than to fill the microporous networks, leaving them permanently dry and available to adsorb gas molecules (Fig. 1a).

Many zeolites and MOFs can be synthesized with hydrophobic pore surfaces and in nanocrystalline form[13–15], making these materials an ideal—and highly tunable—platform to target aqueous solutions with permanent microporosity. Moreover, solid powders of several hydrophobic zeolites and MOFs have been shown to exclude liquid water from their micropores at ambient pressure and temperature[16]. For instance, hydrostatic pressures in excess of 900 bar must be applied to force water into the micropores of the pure-silica zeolite MFI (silicalite-1) at 25 °C (ref. [17]). High pressures are required because water intrusion into silicalite-1 is entropically disfavoured, as confined H_2O molecules have less mobility than bulk H_2O molecules, and endothermic because silicalite-1 pore surface–H_2O interactions are too weak to compensate for the hydrogen bonding interactions between H_2O molecules that are lost during intrusion[18]. Pressures of at least 200 bar are also required to

[1]Department of Chemistry and Chemical Biology, Harvard University, Cambridge, MA, USA. [2]Department of Materials Science and Engineering, Northwestern University, Evanston, IL, USA. [3]Division of Basic Cardiovascular Research, Department of Cardiology, Boston Children's Hospital, Boston, MA, USA. [4]Department of Pediatrics, Harvard Medical School, Boston, MA, USA. [5]Department of Physics and Astronomy, Northwestern University, Evanston, IL, USA. [6]Department of Chemistry, Northwestern University, Evanston, IL, USA. [7]These authors contributed equally: Daniel P. Erdosy, Malia B. Wenny, Joy Cho. ✉e-mail: mason@chemistry.harvard.edu

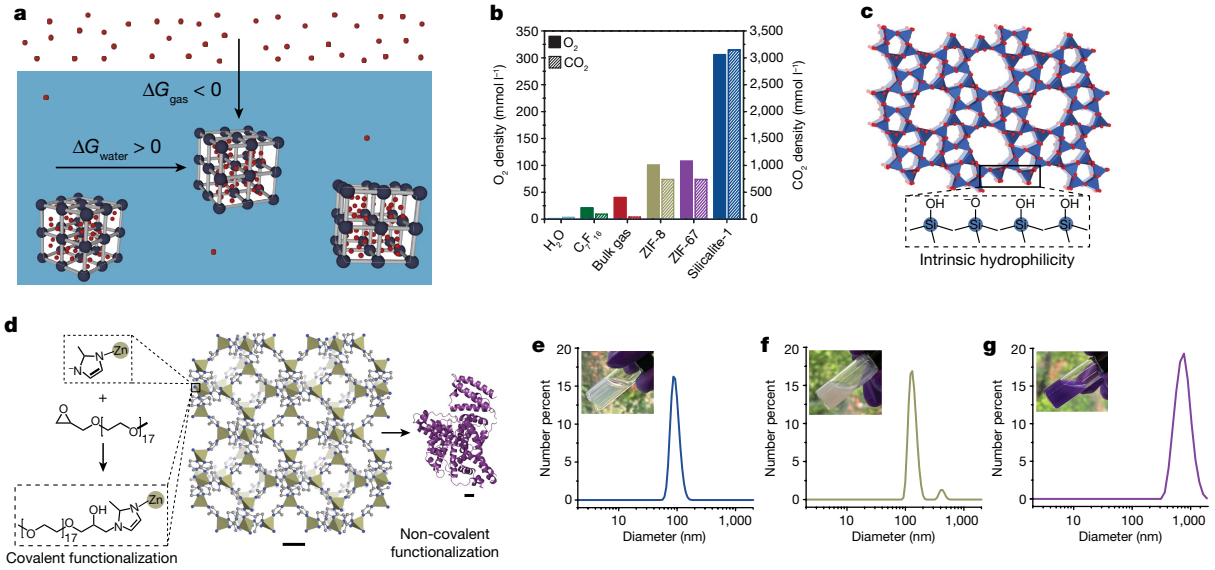

Fig. 1 | Creating aqueous fluids with permanent microporosity. **a**, Illustration of the thermodynamic approach to designing microporous water, whereby microporous nanocrystals with hydrophobic internal surfaces and hydrophilic external surfaces form stable, uniform colloidal solutions in water that contain permanently dry pores capable of adsorbing gas molecules. **b**, The O_2 and CO_2 sorption capacities of two hydrophobic zeolitic imidazolate frameworks (ZIFs) and one hydrophobic zeolite (silicalite-1) are compared with those of pure H_2O, a representative perfluorocarbon solvent (C_7F_{16}) and the density of the bulk gas phase. All O_2 and CO_2 densities are at 1 bar and 25 °C and include the volume occupied by the solid adsorbent or liquid solvent. **c**, Crystal structure of silicalite-1 (ref. [42]). The inset illustrates how the external surface of silicalite-1 is terminated by surface silanol groups and is intrinsically hydrophilic. Blue tetrahedra and red spheres represent Si and O atoms, respectively. **d**, Crystal structure of ZIF-8 (ref. [43]) and an illustration of strategies to increase the hydrophilicity of its external surface through covalent functionalization by means of reaction with hydrophilic epoxides and non-covalent functionalization by means of the adsorption of the protein BSA (Protein Data Bank code 4F5S). Dark yellow tetrahedra, grey spheres and blue spheres represent Zn, C and N atoms, respectively; H atoms are omitted for clarity. Scale bars, 0.5 nm (main image) and 1 nm (right image). **e**–**g**, DLS particle size distributions for aqueous solutions of silicalite-1 (**e**), (mPEG)ZIF-8 (**f**) and BSA/ZIF-67 (**g**). The insets show photos of solutions at nanocrystal concentrations of 12 vol%, 4 vol% and 3 vol%, respectively.

force water into the micropores of other pure-silica zeolites and hydrophobic zeolitic imidazolate frameworks (ZIFs)[16,19]. The work that must be performed to induce water intrusion into hydrophobic microporous solids has been leveraged for mechanical energy storage and shock absorption[17,20], but this phenomenon also offers an unexplored pathway to preserve permanent and accessible microporosity in aqueous solutions—provided that stable colloidal solutions of such materials can be formed in a manner that does not alter the underlying thermodynamic driving force for the constituent microporous networks to remain dry and adsorb gas molecules.

Although hydrophobic materials are not generally dispersible in water, pure-silica zeolites present a unique combination of hydrophobic internal pore surfaces templated by SiO_4 tetrahedra, which should prevent water intrusion, and hydrophilic external surfaces composed of terminal silanol groups, which should promote water dispersibility for sufficiently small particles (Fig. 1c). With an internal Brunauer–Emmett–Teller (BET) surface area of 457 $m^2 g^{-1}$ (839 $m^2 ml^{-1}$) and established routes to produce uniform nanocrystals of variable sizes[21,22] (Extended Data Fig. 3 and Supplementary Fig. 27), we therefore anticipated that silicalite-1 would serve as a particularly promising candidate to generate aqueous solutions with permanent microporosity and high gas capacities. Even though it does not contain any inherently strong gas adsorption sites, silicalite-1 adsorbs more than 230 times the amount of O_2 and 90 times the amount of CO_2 in the solid state as can be dissolved in water on a volumetric basis at 1 bar and 25 °C (Fig. 1b and Supplementary Table 13). In addition, NMR experiments have suggested that at least some fraction of silicalite-1 micropores are accessible to hyperpolarized Xe in water[23].

To create uniform, stable colloidal solutions of silicalite-1 in water and evaluate their permanent microporosity, we first optimized synthesis, purification and calcination conditions to form nanocrystals of similar size (average diameter = 59 ± 8 nm or 90 ± 16 nm) and to remove structure-directing tetrapropylammonium cations from the zeolite micropores without irreversibly aggregating the particles in the solid state (Extended Data Fig. 9). The resulting silicalite-1 nanocrystals yielded translucent aqueous colloidal solutions that were exceptionally stable, with no settling or aggregation observed over the course of at least several weeks (Fig. 1e and Extended Data Fig. 8). Moreover, colloidal stability was not affected by degassing the solutions under vacuum. If the microporous networks of the silicalite-1 nanocrystals in these degassed solutions do not contain water, the most concentrated colloidal solution (25 vol%, 38 wt%) would be 8.3% porous.

Because the volume occupied by a porous liquid with dry (air-filled) micropores will be larger than the volume occupied by an equivalent non-porous liquid with wet (solvent-filled) micropores, density measurements were used as an initial probe of the hydration status of silicalite-1 micropores in colloidal solutions. Excitingly, experimental densities at 15, 25 and 37 °C and across a wide range of silicalite-1 concentrations are within 0.5% of the values predicted for dry micropores using the crystallographic density and measured solid-state pore volume of silicalite-1 (Fig. 2a and Extended Data Fig. 1). These density measurements directly show that the micropores of silicalite-1 nanocrystals are dry in liquid water. We emphasize that liquid water completely surrounds the dispersed nanocrystals—and there would be more than enough water present in solution to fill all framework micropores if it were thermodynamically favourable to do so—at all concentrations investigated. This is in contrast to colloidal solutions of silicalite-1 in ethanol—in which intrusion of the less polar solvent molecules should be thermodynamically favoured at ambient pressure—and of the hydrophilic zeolite LTL in water—in which water intrusion into the more polar

aluminosilicate pores should also be thermodynamically favoured under ambient conditions—which both have densities consistent with non-porous liquids containing solvent-filled micropores (Fig. 2b and Extended Data Fig. 1). Note that the density of solvent within a microporous network is expected to be as much as 40% lower than the bulk liquid density, owing to confinement effects[24]. Moreover, the linear behaviour of the solution density with concentration shows that there is no effect of concentration on pore filling by water; the pores are either empty or filled under these conditions.

For a microporous liquid to be useful for gas storage, separation and transport applications, the pore networks need to be not only dry but also capable of reversibly adsorbing and desorbing gas molecules. To directly investigate the gas accessibility of micropores in water, we measured the amount of O_2 and CO_2 absorbed in degassed solutions. At 25 °C, the gas absorption capacity of a 12 vol% (20 wt%) colloidal solution of silicalite-1 nanocrystals was 26 ± 1 mmol O_2 l^{-1} at 0.84 bar and 284 ± 2 mmol CO_2 l^{-1} at 0.67 bar, which is more than an order of magnitude greater than the 1.1 mmol l^{-1} of O_2 and 23 mmol l^{-1} of CO_2 absorbed in water under the same conditions (Fig. 3a,b). Moreover, these gas capacities are 84% ± 6% and 85% ± 3%, respectively, of the O_2 and CO_2 capacities predicted by assuming that solution absorption is equivalent to the sum of the pure-water gas solubility and the adsorption capacity of silicalite-1 nanocrystals in the solid state (Fig. 3c). Because the solid-state gas capacity measured for nanocrystalline powders will also include contributions from gas adsorption at external surfaces and in interparticle voids that will not be present in solution, these gas capacities are consistent with dry microporous networks in liquid water that are fully accessible to gas molecules (Extended Data Fig. 5). As anticipated, this high gas uptake behaviour is witnessed only for aqueous solutions of hydrophobic nanocrystals; gas sorption experiments for a 5.1 vol% (9.5 wt%) aqueous solution of zeolite LTL nanocrystals show O_2 and CO_2 capacities that are nearly identical to pure water and correspond to less than 2% of the zeolite capacity predicted for dry micropores (Fig. 3). These results emphasize the importance of hydrophobic micropores and permanent microporosity to achieving high gas capacities in water.

Molecular dynamics (MD) simulations further confirm the observed adsorption behaviour for aqueous solutions of hydrophobic silicalite-1 nanocrystals. These simulations show rapid uptake of O_2 in a freely diffusing silicalite-1 nanocrystal that is submerged in liquid water in contact with a bulk O_2 gas phase, in agreement with experimental adsorption kinetics measurements (Fig. 3 and Extended Data Fig. 6). Moreover, MD simulations show that the silicalite-1 nanocrystal pores remain dry while O_2 is adsorbed, and the pores undergo spontaneous and rapid dewetting whenever water molecules are artificially placed inside (Extended Data Fig. 7 and Supplementary Video 1).

Cycling experiments confirm that gas absorption in silicalite-1 colloidal solutions is fully reversible over at least three cycles of absorption followed by desorption under vacuum (Supplementary Fig. 38). In addition, gas desorption was directly quantified by measuring the change in the amount of dissolved O_2 when an oxygenated silicalite-1 solution was injected into pure, degassed water (Fig. 4a). After injection, a partial pressure gradient is established that drives the release of adsorbed O_2 from the silicalite-1 nanocrystals into bulk water. This process continues until the partial pressures of dissolved and adsorbed O_2 are equal and a new equilibrium is established. Consistent with the absorption experiments, oxygenated silicalite-1 solutions deliver up to 86% of the theoretical amount of O_2 predicted from solid-state adsorption isotherms to deoxygenated water (Fig. 4b). Moreover, owing to the labile physisorptive interactions and relatively low viscosity of our solutions, the amount of dissolved O_2 equilibrates within seconds after injection of a silicalite-1 solution, which demonstrates the rapid gas desorption kinetics of these microporous liquids (Fig. 4a).

The thermodynamic approach described here to designing microporous liquids is not specific to silicalite-1 and is generalizable to a wide

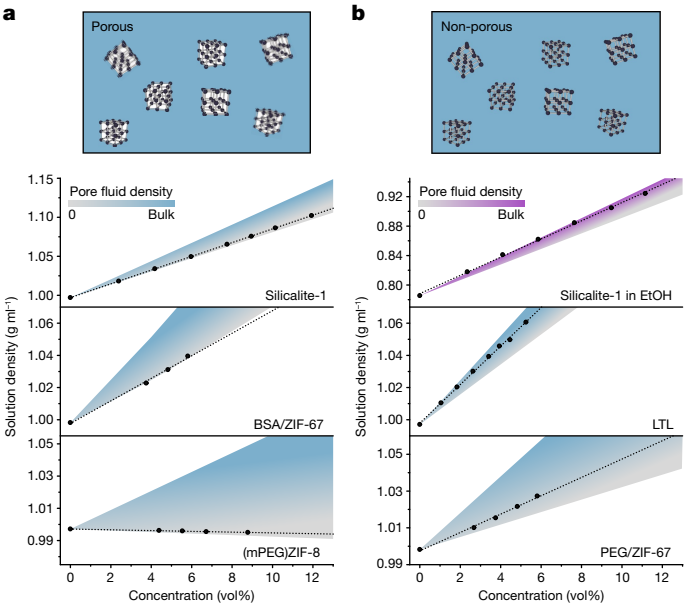

Fig. 2 | Density measurements to evaluate the porosity of aqueous solutions. The density of a porous solution with dry micropores will be lower than the density of an analogous non-porous solution with solvent-filled micropores. The measured densities (black circles) of several microporous nanocrystal colloidal solutions are plotted as a function of nanocrystal concentration at 20 °C (ZIF-67) or 25 °C (all others). Theoretical densities as a function of nanocrystal concentration are indicated by shading, with grey corresponding to a solution with completely dry pores and blue or purple corresponding to a solution with pores filled with aqueous solvent or ethanol (EtOH), respectively, at the same density as the bulk solvent. **a**, The densities of colloidal solutions of silicalite-1, BSA/ZIF-67 and (mPEG)ZIF-8 nanocrystals in water are consistent with microporous fluids containing dry pores. **b**, By contrast, the densities of colloidal solutions of silicalite-1 nanocrystals in EtOH and zeolite LTL and PEG/ZIF-67 nanocrystals in water are consistent with fluids that have no accessible porosity. Note that the density of nanoconfined solvent is often lower than the bulk solvent density[24].

range of hydrophobic microporous materials. For instance, there are now more than 50 known pure-silica zeolites and many other high-silica zeolites that should be hydrophobic enough to exclude water in colloidal solutions[25]. Beyond zeolites, MOFs offer access to even higher internal surface areas and gas capacities, along with substantially more structural and chemical diversity[26]. Most hydrophobic MOFs, however, have relatively hydrophobic external surfaces and are not inherently dispersible in water. Many hydrophobic MOFs are also prone to degradation in water particularly at low concentrations. This is true for the isostructural hydrophobic frameworks $Zn(mIm)_2$ (ZIF-8; mIm = 2-methylimidazolate[27]) and $Co(mIm)_2$ (ZIF-67) (Fig. 1d)—nanocrystals of which rapidly aggregate in water and may degrade if a large excess of water is present. Surface functionalization strategies can be applied to disperse and stabilize hydrophobic MOFs in water[28,29], providing a route to aqueous MOF solutions with permanent microporosity, as long as surface ligands can be selected that promote dispersibility without infiltrating—or blocking access to—the framework micropores.

Non-covalent surface functionalization with macromolecules such as polyethylene glycol (PEG) represents a simple approach for dispersing nanocrystals in solvents that would otherwise induce aggregation and precipitation. Although ZIF-8 microparticles were previously shown to aggregate rapidly in liquid PEG (M_n = 500 g mol^{-1})[30], we found that PEG (M_n = 35,000 g mol^{-1}) at 30 wt% can disperse at least 20 wt% (21 vol%) of ZIF-8 nanocrystals (average size = 103 ± 10 nm) and 7.0 wt% (7.4 vol%) of ZIF-67 particles (average size = 780 ± 120 nm) in water without

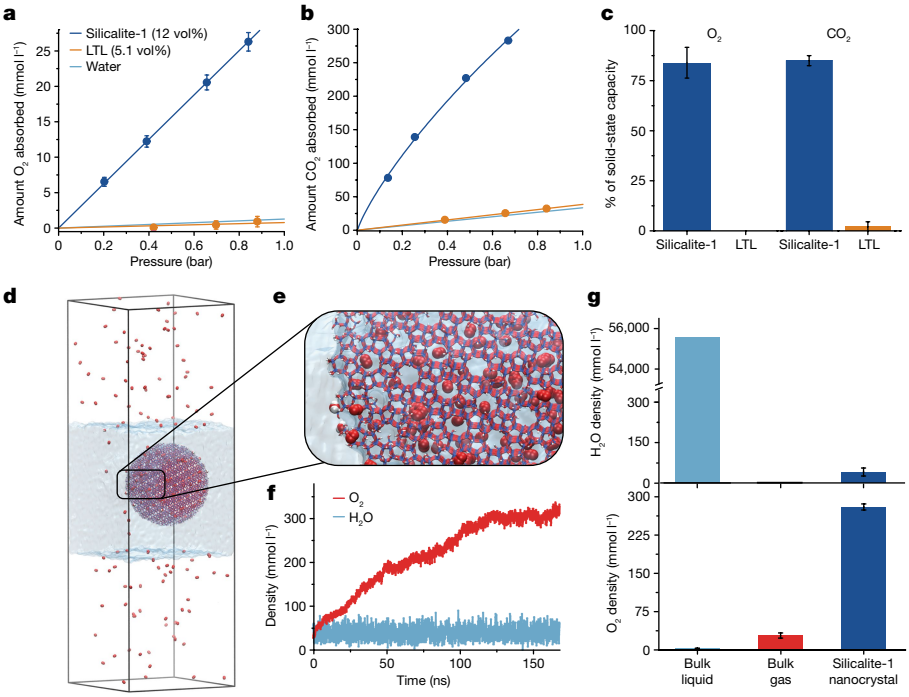

Fig. 3 | Equilibrium gas sorption isotherms and MD simulations. Gas absorption isotherms for O_2 (**a**) and CO_2 (**b**) in a 12.2 vol% solution of silicalite-1 nanocrystals in water (navy) and a 5.1 vol% solution of zeolite LTL nanocrystals in water (orange) at 25 °C. Navy and orange lines represent linear fits to the isotherm data, with the exception of a single-site Langmuir–Freundlich fit for CO_2 absorption in the silicalite-1 solution. The O_2 and CO_2 solubilities of pure water at 25 °C are indicated with light blue lines. Error bars represent the standard deviations associated with pure-water control experiments (Supplementary Tables 14–16); note that the error bars are smaller than the size of the data point in some cases. **c**, The amount of O_2 and CO_2 adsorbed by the zeolite nanocrystals in aqueous solution, which is obtained by accounting for the pure-water gas solubility, relative to the zeolite solid-state gas capacities. Error bars represent the standard deviations associated with pure-water control experiments (Supplementary Tables 14–16). **d**, An image of the 16.2 × 16.2 × 52 nm simulation box used for MD simulations containing a spherical nanocrystal of silicalite-1 initially filled with 3,500 H_2O molecules and surrounded by a bulk water phase and a headspace of O_2 gas molecules. The snapshot of the simulation box is of the system after equilibration and expulsion of internal H_2O molecules. O atoms are shown in red, H atoms in white and Si atoms in blue, whereas the bulk water phase is represented as a semi-transparent blue volume. **e**, A zoomed-in view of the silicalite-1 nanocrystal edge. **f**, The change in density of O_2 and H_2O inside an initially dry silicalite-1 nanocrystal over the timescale of the simulation. **g**, The average concentrations of H_2O (top) and O_2 (bottom) during the last 50 ns of the simulation in the bulk liquid phase, bulk gas phase and silicalite-1 nanocrystal.

observable aggregation. Furthermore, ZIF-8 remains crystalline when associated with PEG in water for at least 5 weeks, and PEG increases the hydrolytic stability of ZIF-67, which otherwise rapidly degrades in water (Supplementary Figs. 4 and 48). However, the measured O_2 capacities of the PEG/ZIF-8 and PEG/ZIF-67 colloidal solutions are less than 10% of the expected capacities for solutions of ZIF particles containing empty and accessible microporous networks (Fig. 4b). Along with density measurements (Fig. 2b), these limited O_2 capacities suggest that the colloidal PEG/ZIF solutions are not porous because of PEG—and perhaps H_2O—intrusion into the ZIF micropores. Given that PEG is a compact, flexible polymer and is amphiphilic, there does not seem to be a strong enough driving force to prevent its intrusion by either sterics or thermodynamics, which is consistent with observations in the solid state for PEG with other MOFs[31].

As an alternative to synthetic polymers, we anticipated that globular water-soluble proteins could serve as promising macromolecules for non-covalent ZIF surface functionalization owing to their large size, conformational rigidity and propensity to adsorb on hydrophobic surfaces[32]. We identified bovine serum albumin (BSA) as an initial target for adsorbing onto ZIF-8 and ZIF-67 external surfaces because of its large diameter (about 7 nm) and 17 permanent disulfide linkages that minimize its conformational flexibility—the combination of which should sterically preclude protein intrusion into the ZIF framework and preserve permanent microporosity (Fig. 1d). As anticipated, mixing BSA (10 wt%) with ZIF-67 particles (3.3 wt%) enables complete dispersion of ZIF-67 in water with no observable precipitation over a period of at least 8 days (Fig. 1g and Supplementary Fig. 48), and density measurements are consistent with air-filled pores (Fig. 2a). Moreover, the measured O_2 capacities of BSA/ZIF-67 colloidal solutions are 80% ± 9% of the theoretical capacities obtained by assuming that all ZIF-67 pores are empty and accessible to gas molecules (Fig. 4a,b). Spectroscopic analysis and MD simulations confirm that the secondary structure of BSA prevents global unfolding and pore infiltration after BSA adsorbs to the ZIF-67 surface (Extended Data Fig. 7, Supplementary Fig. 49 and Supplementary Video 2). Moreover, simulations confirm that ZIF-67 pores remain dry and capable of adsorbing O_2 molecules when surrounded by liquid water (Supplementary Video 3). As well as promoting dispersibility, BSA stabilizes ZIF-67 nanocrystals, which rapidly degrade in water in the absence of BSA (Supplementary Fig. 48). Specifically, we observe just 8.2% degradation and negligible change in O_2 capacity (85% ± 2% of theoretical) after 1 week in water for a BSA:ZIF-67 ratio of 2.5:1 (Supplementary Tables 35 and 49). At a BSA:ZIF-67 ratio of 6:1, we observe 102% ± 5% of the theoretical O_2 capacity after 1 week in water, which is indicative of even greater stabilization. Thus, non-covalent protein adsorption successfully extends the microporous water concept to hydrophobic MOFs.

Aside from non-covalent approaches, covalent surface functionalization offers the potential for strongly bound and precisely located surface ligands that promote water dispersibility at lower loadings than more weakly associated surface ligands[29,33] (Fig. 1). For covalent functionalization to lead to an aqueous microporous liquid, the surface ligand must be hydrophilic enough—and present at a high enough

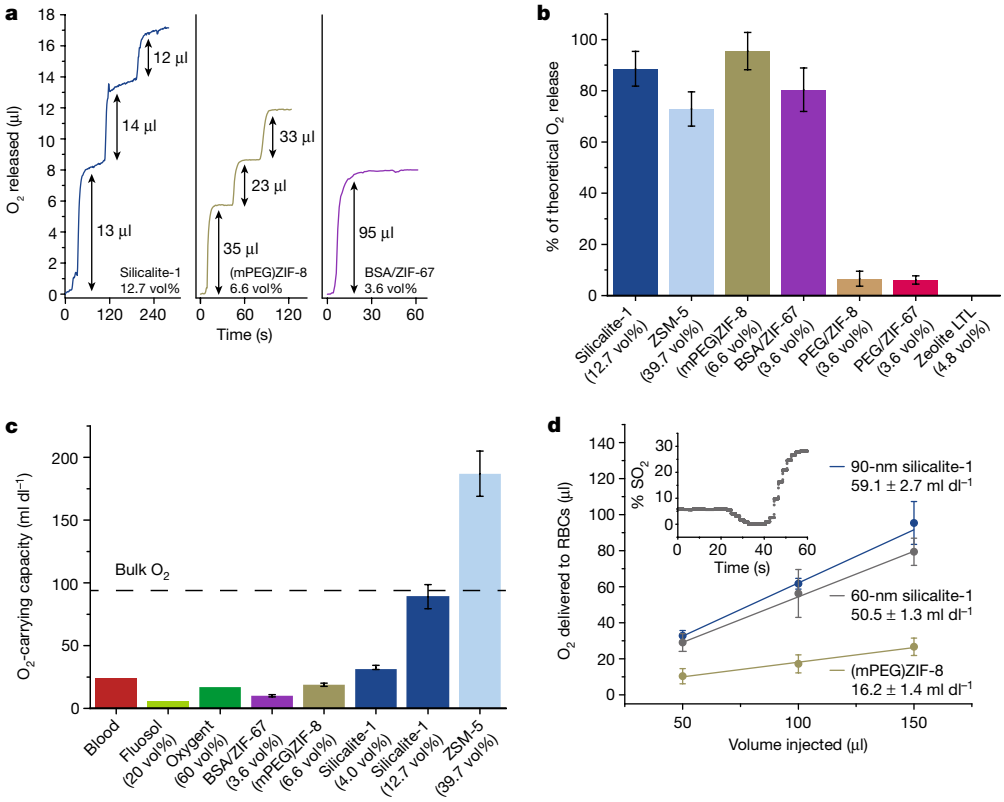

Fig. 4 | O_2 release measurements in water and blood. a, O_2 release kinetics for injections of oxygenated silicalite-1, (mPEG)ZIF-8 and BSA/ZIF-67 nanocrystal solutions into deoxygenated water. All solutions were injected into a 1.2-ml gas-tight vial, and the injection volumes are indicated next to the arrows. **b**, The amount of O_2 delivered by oxygenated aqueous solutions of hydrophobic zeolite and MOF nanocrystals relative to the theoretical amount calculated by assuming fully dry pores with gas capacities equivalent to those measured in the solid state. **c**, Comparison of the O_2-carrying capacities of aqueous solutions of hydrophobic zeolite and MOF nanocrystals to the O_2-carrying capacities of blood (15 g Hb dl^{-1}) and two representative perfluorocarbon emulsions (Fluosol and Oxygent). All capacities are for solutions equilibrated at 1 bar O_2 near ambient temperature. **d**, The amount of O_2 delivered to deoxygenated packed red blood cells (RBCs) by oxygenated solutions of (mPEG)ZIF-8 (6.7 vol%) and silicalite-1 nanocrystals (9.1 vol% and 11.0 vol% for 60-nm and 90-nm nanocrystals, respectively) as a function of the volume of solution injected. The O_2 capacities of each solution are calculated from the slope of linear fits to the data. Note that all solutions were equilibrated at 1 bar O_2 at ambient temperature and contain 5% dextrose. Inset, representative O_2 release kinetics for a single injection of 100 μl solution of 60-nm silicalite-1 nanocrystals (9.1 vol%). The baseline was collected for at least 4 min prior to injection to ensure stabilization of the O_2 sensor. Error bars in **b**–**d** represent the standard deviation associated with at least three independent measurements for each data point.

density—to promote water dispersibility, although short enough or bulky enough to prevent pore infiltration. Moreover, functionalization must be confined to the external surface of the nanocrystal and not inhibit gas accessibility to the internal pore surfaces. Although functionalization with carbene surface ligands has been used to disperse ZIF nanocrystals in large cyclic organic solvents to form organic microporous liquids[34], the reactivity of carbenes makes this synthetic strategy difficult to adapt to water. As an alternative approach, we anticipated that mIm surface ligands would be nucleophilic enough to open epoxide rings and form a β-hydroxyalkyl covalent linkage to the ZIF surface[35] (Fig. 1d). On the basis of this reasoning, we reacted ZIF-8 nanocrystals with methoxypolyethylene epoxide (mPEG; M_n = 750 g mol^{-1} for PEG). The formation of the expected covalent linkage between the ring-opened epoxide and mIm was confirmed by mass spectrometry (Supplementary Fig. 51), with NMR digestion experiments indicating that approximately 10% of the mIm surface ligands are functionalized with mPEG (Supplementary Fig. 52). Notably, this grafting density (0.8 ligands per nm^2) is sufficient to stabilize colloidal solutions of ZIF-8 in water at up to 8.3 vol% (7.0 wt%), with minimal precipitation or aggregation over the course of at least 5 days (Fig. 1f and Extended Data Fig. 8c). By contrast to ZIF-8 nanocrystals non-covalently functionalized with PEG, the solution density as a function of concentration is consistent with that expected for a microporous liquid containing air-filled pores (Fig. 2a), and the measured O_2 capacity is 96% ± 7% of the theoretical amount (Fig. 4a,b). Thus, covalent surface modification with low-molecular-weight ligands can impart colloidal dispersibility of hydrophobic MOFs in water while maintaining permanent microporosity and high gas absorption capacities.

The high gas capacities of the microporous liquids reported here present intriguing possibilities for in vitro or in vivo O_2 delivery, among others. Nature evolved intricate and tightly regulated systems to transport O_2 in water over hundreds of millions of years, and it is challenging to deliver enough O_2 to prevent hypoxia when these systems are absent or fail. A variety of natural and synthetic gas carriers—including cell-free haemoglobin, haem mimics, perfluorocarbon emulsions and lipid-coated or polymer-coated microbubbles—have been explored to deliver O_2 from aqueous fluids, but overcoming issues that include limited gas-carrying capacity, poor control over release kinetics, lack of reversibility, large particle sizes, dose-limiting toxicity and long-term stability remains an unsolved challenge[6,36]. As a result, there are—at present—no injectable sources of O_2 or artificial blood substitutes approved by the U.S. Food and Drug Administration, despite decades of research.

When oxygenated at 1 bar and 25 °C, blood has an O_2-carrying capacity of around 24 ml dl^{-1} (assuming 15 g Hb dl^{-1}), which is an order of magnitude larger than the 2.9 ml dl^{-1} that can be dissolved in pure H_2O.

Among non-covalent O_2 carriers, lipid-coated microbubble dispersions (90 vol%) have been demonstrated with irreversible O_2 capacities that approach the gas-phase density of O_2 (91 ml dl^{-1}), whereas concentrated perfluorocarbon emulsions (60 vol%) have reached reversible O_2 capacities as high as 17 ml dl^{-1} (refs. [36,37]) (Fig. 4c). Microporous liquids offer a pathway to reversible O_2 capacities that far exceed these values, which would allow larger amounts of O_2 to be delivered from smaller volumes of an aqueous fluid. In particular, as silicalite-1 and ZIF-8 nanocrystals adsorb 731 ml dl^{-1} and 241 ml dl^{-1} of O_2, respectively, in the solid state, low-concentration aqueous solutions should be able to store and deliver exceptionally high densities of O_2. Indeed, a 6.6 vol% solution of (mPEG)ZIF-8 nanocrystals has a measured O_2-carrying capacity that is similar to many perfluorocarbon emulsions, which have concentrations of at least 20 vol% (Fig. 4c). Moreover, at a concentration of just 4.0 vol%, our aqueous solution of 90-nm silicalite-1 nanocrystals has a measured reversible O_2 capacity of 31.3 ± 0.1 ml dl^{-1}, exceeding that of blood (Extended Data Table 1). At a concentration of 12.7 vol%, this O_2-carrying capacity increases to 89 ± 10 ml dl^{-1}, which is comparable with the density of bulk O_2 gas (Fig. 4b). Although higher concentration solutions of silicalite-1 nanocrystals tended to gel, we found that nanocrystals of the zeolite ZSM-5—which is the isostructural aluminosilicate analogue of silicalite-1—have more hydrophilic external surfaces than silicalite-1 nanocrystals (the zeta potentials of ZSM-5 and silicalite-1 are −49.1 mV and −38.7 mV, respectively). As a result, we were able to form a stable colloidal solution of ZSM-5 nanocrystals (average diameter = 193 ± 32 nm; Si/Al ratio = 64) in water at a concentration of up to 40 vol%, with relatively low viscosities even at high concentrations (Extended Data Fig. 2). Moreover, density measurements confirmed that the micropores are hydrophobic enough at this high Si/Al ratio to prevent water intrusion and form a microporous solution. This leads to an extremely high measured O_2-carrying capacity of 187 ± 18 ml dl^{-1} that, to the best of our knowledge, far exceeds the capacity of any other natural or synthetic aqueous O_2 carrier (Fig. 4c).

As an initial exploration of whether the high O_2-carrying capacities of these microporous liquids could be translated to more biomedically relevant environments than pure water, we performed ex vivo experiments to test the delivery of O_2 to deoxygenated donated human blood. Notably, density measurements confirm that the permanent microporosity of silicalite-1 and (mPEG)ZIF-8 nanocrystals is maintained in a 5% dextrose solution (Extended Data Fig. 1), which is isosmotic to red blood cells. The O_2-carrying capacity of these solutions was extracted from measurement of the change in oxyhaemoglobin concentration on addition of different volumes of oxygenated solutions to deoxygenated red blood cells. Notably, oxygenated solutions of 90-nm silicalite-1 nanocrystals (11.0 vol%), 60-nm silicalite-1 nanocrystals (9.1 vol%) and (mPEG)ZIF-8 (6.6 vol%) in 5% dextrose rapidly release O_2 after injection into red blood cells, with the amount of O_2 released increasing linearly in a dose-dependent manner. The extracted O_2-carrying capacities are in excellent agreement with the values predicted from adsorption measurements and O_2-release experiments in pure water (Fig. 4c,d). Furthermore, more concentrated silicalite-1 colloidal solutions were capable of delivering 110 ml dl^{-1} of O_2 to red blood cells (Supplementary Table 45). These proof-of-principle experiments demonstrate the potential of aqueous microporous liquids for in vivo or in vitro O_2 delivery, but we note that many other factors—including cyclability, biocompatibility, long-term stability and cost—will need to be considered when designing a fluid to meet the requirements of a particular biomedical application.

Overall, our results show how thermodynamic principles can be applied to bring the high surface areas and gas capacities of microporous solids to aqueous fluids. This approach has notable implications for biomedical and energy technologies, many of which are limited by the transport of gas molecules through aqueous environments. For instance, the microporous water concept could lead to new electrolytes that complement or replace gas-diffusion electrodes in electrocatalytic reactions[7] or overcome mass-transport limitation in fuel cells using dilute gas streams[8] by allowing a higher density of gas molecules to be localized near the electrode surface—effectively serving as a gas buffer. Beyond catalysis and energy storage, aqueous microporous liquids have potential as green solvents for acid gas separations[38], as these fluids offer opportunities for higher gas solubilities, lower cost and less harmful environmental effects compared with existing organic solvents systems used in physisorptive processes. On the biomedical front, microporous water could enable treatments for decompression sickness[39] or serve as sources of O_2 for artificial blood substitutes[36], bridge therapies for hypoxia induced by trauma[40] or media for organ and tissue preservation[41]. Although many factors beyond gas-carrying capacity need to be considered to translate these systems to viable technologies, there are myriad possibilities for designing hydrophobic zeolites and MOFs with different crystal structures, nanocrystal sizes and shapes, and external surface functional groups to create microporous water with high gas capacities and properties tailored to a specific application.

Online content

Any methods, additional references, Nature Research reporting summaries, source data, extended data, supplementary information, acknowledgements, peer review information; details of author contributions and competing interests; and statements of data and code availability are available at https://doi.org/10.1038/s41586-022-05029-w.

1. Giri, N. et al. Liquids with permanent porosity. *Nature* **527**, 216–220 (2015).
2. Bavykina, A., Cadiau, A. & Gascon, J. Porous liquids based on porous cages, metal organic frameworks and metal organic polyhedra. *Coord. Chem. Rev.* **386**, 85–95 (2019).
3. Jie, K., Zhou, Y., Ryan, H. P., Dai, S. & Nitschke, J. R. Engineering permanent porosity into liquids. *Adv. Mater.* **33**, 2005745 (2021).
4. Bennett, T. D., Coudert, F.-X., James, S. L. & Cooper, A. I. The changing state of porous materials. *Nat. Mater.* **20**, 1179–1187 (2021).
5. Wilhelm, E., Battino, R. & Wilcock, R. J. Low-pressure solubility of gases in liquid water. *Chem. Rev.* **77**, 219–262 (1977).
6. Peng, Y., Kheir, J. N. & Polizzotti, B. D. Injectable oxygen: interfacing materials chemistry with resuscitative science. *Chem. Eur. J.* **24**, 18820–18829 (2018).
7. Rabiee, H. et al. Gas diffusion electrodes (GDEs) for electrochemical reduction of carbon dioxide, carbon monoxide, and dinitrogen to value-added products: a review. *Energy Environ. Sci.* **14**, 1959–2008 (2021).
8. Fox E. B. & Colón-Mercardo, H. R. in *Mass Transfer–Advanced Aspects* (Ed. Nakajima, H.) Ch. 13 (Intech, 2011).
9. Morris, R. E. & Wheatley, P. S. Gas storage in nanoporous materials. *Angew. Chem. Int. Ed.* **47**, 4966–4981 (2008).
10. Greenaway, R. L. et al. Understanding gas capacity, guest selectivity, and diffusion in porous liquids. *Chem. Sci.* **8**, 2640–2651 (2017).
11. Matthews, B. W. & Liu, L. A review about nothing: are apolar cavities in proteins really empty? *Protein Sci.* **18**, 494–502 (2009).
12. Barnett, J. W. et al. Spontaneous drying of non-polar deep-cavity cavitand pockets in aqueous solution. *Nat. Chem.* **12**, 589–594 (2020).
13. Mintova, S., Gilson, J. P. & Valtchev, V. Advances in nanosized zeolites. *Nanoscale* **5**, 6693–6703 (2013).
14. Sindoro, M., Yanai, N., Jee, A. Y. & Granick, S. Colloidal-sized metal–organic frameworks: synthesis and applications. *Acc. Chem. Res.* **47**, 459–469 (2014).
15. Jayaramulu, K. et al. Hydrophobic metal–organic frameworks. *Adv. Mater.* **31**, 1900820 (2019).
16. Fraux, G., Coudert, F. X., Boutin, A. & Fuchs, A. H. Forced intrusion of water and aqueous solutions in microporous materials: from fundamental thermodynamics to energy storage devices. *Chem. Soc. Rev.* **46**, 7421–7437 (2017).
17. Eroshenko, V., Regis, R.-C., Soulard, M. & Patarin, J. Energetics: a new field of applications for hydrophobic zeolites. *J. Am. Chem. Soc.* **123**, 8129–8130 (2001).
18. Cailliez, F. et al. Thermodynamics of water intrusion in nanoporous hydrophobic solids. *Phys. Chem. Chem. Phys.* **10**, 4817–4826 (2008).
19. Ortiz, G., Nouali, H., Marichal, C., Chaplais, G. & Patarin, J. Energetic performances of the metal–organic framework ZIF-8 obtained using high pressure water intrusion–extrusion experiments. *Phys. Chem. Chem. Phys.* **15**, 48884888 (2013).
20. Khay, I. et al. Assessment of the energetic performances of various ZIFs with SOD or RHO topology using high pressure water intrusion–extrusion experiments. *Dalton Trans.* **45**, 4392–4400 (2016).
21. Flanigen, E. M. et al. Silicalite, a new hydrophobic crystalline silica molecular sieve. *Nature* **271**, 512–516 (1978).
22. Persson, A. E., Schoeman, B. J., Sterte, J. & Otterstedt, J. E. The synthesis of discrete colloidal particles of TPA-silicalite-1. *Zeolites* **14**, 557–567 (1994).
23. Lerouge, F. et al. Towards thrombosis-targeted zeolite nanoparticles for laser-polarized ^{129}Xe MRI. *J. Mater. Chem.* **19**, 379–386 (2008).

24. Desbiens, N. et al. Water condensation in hydrophobic nanopores. *Angew. Chem. Int. Ed.* **44**, 5310–5313 (2005).
25. Mazur, M. et al. Synthesis of 'unfeasible' zeolites. *Nat. Chem.* **8**, 58–62 (2016).
26. Furukawa, H., Cordova, K. E., O'Keeffe, M. & Yaghi, O. M. The chemistry and applications of metal-organic frameworks. *Science* **341**, 1230444 (2013).
27. Park, K. S. et al. Exceptional chemical and thermal stability of zeolitic imidazolate frameworks. *Proc. Natl Acad. Sci.* **103**, 10186–10191 (2006).
28. Rocca, J. D., Liu, D. & Lin, W. Nanoscale metal–organic frameworks for biomedical imaging and drug delivery. *Acc. Chem. Res.* **44**, 957–968 (2011).
29. McGuire, C. V. & Forgan, R. S. The surface chemistry of metal–organic frameworks. *Chem. Commun.* **51**, 5199–5217 (2015).
30. Gomes, M. C., Pison, L., Červinka, C. & Padua, A. Porous ionic liquids or liquid metal–organic frameworks? *Angew. Chem. Int. Ed.* **130**, 12085–12088 (2018).
31. Duan, P. et al. Polymer infiltration into metal–organic frameworks in mixed-matrix membranes detected in situ by NMR. *J. Am. Chem. Soc.* **141**, 7589–7595 (2019).
32. Beverung, C. J., Radke, C. J. & Blanch, H. W. Protein adsorption at the oil/water interface: characterization of adsorption kinetics by dynamic interfacial tension measurements. *Biophys. Chem.* **81**, 59–80 (1999).
33. Wang, S. et al. Surface-specific functionalization of nanoscale metal-organic frameworks. *Angew. Chem. Int. Ed.* **54**, 14738–14742 (2015).
34. Knebel, A. et al. Solution processable metal–organic frameworks for mixed matrix membranes using porous liquids. *Nat. Mater.* **19**, 1346–1353 (2020).
35. Kühl, O. The chemistry of functionalised *N*-heterocyclic carbenes. *Chem. Soc. Rev.* **36**, 592–607 (2006).
36. Riess, J. G. Oxygen carriers ("blood substitutes") – raison d'etre, chemistry, and some physiology. *Chem. Rev.* **101**, 2797–2919 (2001).
37. Kheir, J. N. et al. Oxygen gas-filled microparticles provide intravenous oxygen delivery. *Sci. Transl. Med.* **4**, 140ra88 (2012).
38. Heintz, Y. J., Sehabiague, L., Morsi, B. I., Jones, K. L. & Pennline, H. W. Novel physical solvents for selective CO_2 capture from fuel gas streams at elevated pressures and temperatures. *Energy Fuels* **22**, 3824–3837 (2008).
39. Mayer, D. & Ferenz, K. B. Perfluorocarbons for the treatment of decompression illness: how to bridge the gap between theory and practice. *Eur. J. Appl. Physiol.* **119**, 2421–2433 (2019).
40. Eisenburger, P. et al. Cardiac arrest in public locations—an independent predictor for better outcome? *Resuscitation* **70**, 395–403 (2006).
41. Farris, A. L., Rindone, A. N. & Grayson, W. L. Oxygen delivering biomaterials for tissue engineering. *J. Mater. Chem. B* **4**, 3422–3432 (2016).
42. Baerlocher, C. & McCusker, L. B. *Database of Zeolite Structures* (Structure Commission of the International Zeolite Association, accessed 31 August 2021); http://www.iza-structure.org/databases/.
43. Morris, W. et al. NMR and X-ray study revealing the rigidity of zeolitic imidazolate frameworks. *J. Phys. Chem. C* **116**, 13307–13312 (2012).

Methods

General procedures

Nanopure H_2O was obtained using a Milli-Q IQ 7000 water purification system. All compounds were synthesized and handled in air. All reagents were purchased from commercial vendors and used as received. Ultrahigh-purity grade (99.999% purity) He, O_2 and CO_2 were used for all gas sorption measurements. Hydrothermal syntheses were performed in Parr acid digestion vessels with polytetrafluoroethylene liners. Sonication was performed using a 0.5-gallon Branson CPX series sonicator with an operating frequency of 40 kHz. Calcination was performed using a STF1200 Across International tube furnace. Powder X-ray diffraction patterns were measured at ambient temperature using a D2 PHASER Bruker AXS diffractometer with CuKα radiation (λ = 1.5418 Å).

Material synthesis

Synthesis of 90-nm silicalite-1 nanocrystals. Silicalite-1 nanocrystals with an average diameter of 90 nm were synthesized following a procedure adapted from a previous report[22]. In a representative synthesis, aqueous tetrapropylammonium hydroxide (TPAOH; 31.51 ml, 40 wt%), H_2O (40.52 ml) and tetraethylorthosilicate (TEOS; 38.36 ml) were combined in a 250-ml glass bottle. The initially biphasic mixture was stirred for 18 h, allowing the TEOS to become hydrolysed in the alkaline environment and liberate ethanol (EtOH) into the solution. Following hydrolysis, the molar ratio of this solution was 9 TPAOH:25 SiO_2:480 H_2O:100 EtOH. The homogenous solution was loaded into a combination of 23-ml and 45-ml Parr acid digestion vessels, with each vessel filled to about 50% with the solution. These were sealed and heated to 90 °C for 48 h. After allowing the vessels to cool, the product was diluted roughly tenfold with nanopure H_2O and centrifuged at 7,830 revolutions per minute (rpm) (7,197 relative centrifugal force (rcf)) for 80 min. The supernatant was then removed and washed six times with nanopure H_2O. After the final wash, the sample was dried in a centrifuge tube at 60 °C overnight. The dried sample was collected and finely ground into a powder. About 3 g of powder was poured into alumina crucibles and loaded into a tube furnace. The powder was dried under flowing N_2 by heating to 200 °C over 1 h and holding at this temperature for a further 2 h. The powder was then calcined by heating to 550 °C over 1 h under flowing air and holding at this temperature for 10 h. The sample was then cooled to ambient temperature and collected.

Synthesis of 60-nm silicalite-1 nanocrystals. In a representative synthesis, aqueous TPAOH (53.35 ml, 40 wt%) and TEOS (64.46 ml) were combined in a 250-ml glass bottle. The biphasic mixture was stirred for 68 h to allow for full hydrolysis of TEOS and ageing of the solution. The molar ratio of the resulting solution was 9 TPAOH:25 SiO_2:380 H_2O:100 EtOH. On completion of ageing, the solution was then uncapped and placed in an oil bath at 110 °C to evaporate the EtOH generated during hydrolysis of TEOS. Over the course of 2 h, the oil bath temperature was raised to 120 °C. After heating, the solution was reweighed and H_2O was added to replace H_2O that evaporated during heating and bring the molar ratio of the solution to 9 TPAOH:25 SiO_2:280 H_2O. The resulting homogenous solution was loaded into 23-ml Parr acid digestion vessels, with each vessel filled to about 50% with the solution. These were sealed and heated to 80 °C for 48 h. After allowing the vessels to cool, the product was diluted roughly tenfold with nanopure H_2O and washed six times with nanopure H_2O after centrifuging at 7,830 rpm (7,197 rcf) for 180 min and removing the supernatant. After the final wash, the sample was dried in a centrifuge tube at 60 °C overnight. The dried sample was collected, finely ground into a powder and calcined following the same procedure as described for the 90-nm silicalite-1 nanoparticles.

Synthesis of high-silica ZSM-5 nanocrystals. ZSM-5 nanocrystals were synthesized following a procedure adapted from a previous report[44]. In a representative synthesis, aqueous TPAOH (5.55 ml, 20.3 wt%) and H_2O (17.904 ml) were combined in a 250-ml glass bottle. While stirring, TEOS (27.104 ml) was added. Simultaneously, aluminium isopropoxide (495.8 mg), TPAOH (16.664 ml), H_2O (5.968 ml) and NaOH (0.408 ml, 2.4 M) were added to a 50-ml round-bottom flask. The mixture was capped with a septum and heated while stirring at 85 °C until all the aluminium isopropoxide was dissolved. The Al solution was then cooled to room temperature and added dropwise to the Si solution while stirring. The resulting solution was then aged for 24 h at room temperature with stirring. After ageing, the molar ratio of the resulting solution was 4.6 TPAOH:0.1 Na_2O:25 SiO_2:0.25 Al_2O_3:482 H_2O:100 EtOH. The solution was then partitioned into three 23-ml and two 45-ml Parr acid digestion vessels and heated to 90 °C for 60 h while rotating, with each vessel filled to about 50% with the solution. After allowing the vessels to cool, the product was divided evenly between six centrifuge tubes, diluted with nanopure H_2O and washed 12 times by centrifuging at 7,830 rpm (7,197 rcf) for 15 min. After the final wash, the sample was dried in centrifuge tubes at 60 °C overnight. The dried sample was collected, finely ground into a powder and calcined following the same procedure as described for the 90-nm silicalite-1 nanocrystals. The final Si/Al ratio was 64 and the Al/Na ratio was 3.7, as determined by inductively coupled plasma atomic emission spectroscopy (ICP-AES) by Galbraith Laboratories.

Synthesis of zeolite LTL nanocrystals. In a representative synthesis adapted and modified from a previous report[45], KOH (14.14 g, 0.252 mol) was added to H_2O (45 ml) in a 100-ml glass jar with a polytetrafluoroethylene stir bar. Then, $Al(OH)_3$ (2.43 g, 0.031 mol) was added to the solution and dissolved by heating to 105 °C for 2.75 h, after which the solution became clear. The solution was cooled to ambient temperature, then HS-40 LUDOX (40%, 28.60 ml) was added while stirring. Within 30 min, the homogenous solution thickened and became opaque. The solution was left to age overnight with stirring, after which the solution became fluid again and had a moderately translucent blue hue. The solution was then loaded into 23-ml Parr acid digestion vessels, with each vessel filled to about 50% with the solution. The vessels were subsequently sealed and heated to 180 °C for 73 h, with each vessel filled to 40% with the solution. The product was diluted roughly tenfold with nanopure H_2O and washed 15 times with nanopure H_2O after centrifuging at 7,830 rpm (7,197 rcf) for 180 min and removing the supernatant. After completion of the washes, the zeolite LTL nanoparticles were redispersed in enough H_2O to bring the volumetric concentration to 9 vol%. The Si:Al ratio was 2.6:1 and the Al:K ratio was 1.1:1, as determined by ICP-AES by Galbraith Laboratories.

Formation of aqueous solutions of silicalite-1 nanocrystals. To create uniform and stable colloidal dispersions, H_2O (13.5 ml) was added to calcined 60-nm or 90-nm silicalite-1 nanocrystals (4.45 g) in a 20-ml glass vial sealed with a Teflon cap and sonicated for up to 1 week. Following sonication, the mostly translucent dispersion was transferred into a 50-ml centrifuge tube for further purification. The goal of this subsequent step was to remove any large aggregates that had irreversibly fused during calcination. To do so, the dispersion was subjected to a total of 25 centrifugation cycles; following each round of centrifugation, the supernatant was decanted and transferred to a fresh tube. The dispersion was first centrifuged at 1,500 rpm (264 rcf) for 15 min to remove any large agglomerates, then centrifuged at 7,830 rpm (7,197 rcf) for 24 cycles ranging from 30 s to 1 min in duration. To concentrate the solution, the sample was split into two tubes and spun at 7,197 rcf for 15 min to generate a nanoparticle-free layer of H_2O on top. The final concentration of the solution could be tuned by removing different amounts of H_2O before redispersing the nanocrystals.

Formation of aqueous solutions of ZSM-5 nanocrystals. To create uniform colloidal dispersions, H_2O was added to calcined ZSM-5 nanocrystals (about 3 g) in a 20-ml glass vial sealed with a Teflon cap

and sonicated for a few days. Following sonication, the milky dispersion was transferred into a 50-ml centrifuge tube. The particles were washed three times with nanopure H_2O at 7,830 rpm (7,197 rcf). Following washing, the particles were then size selected by centrifuging twice at 1,500 rpm (264 rcf) for 15 min and discarding the precipitate. The dispersion was then repeatedly centrifuged for 2 min at 7,830 rpm (7,197 rcf), decanting the supernatant each time. A small amount of nanopure H_2O was then added to the precipitate.

Synthesis of ZIF-8 nanocrystals. ZIF-8 was synthesized in methanol (MeOH) following a previously reported procedure[46]. Briefly, $Zn(NO_3)_2{\cdot}6H_2O$ (2.9 g, 0.0097 mol) and 2-methylimidazole (mIm; 6.5 g, 0.079 mol) were each dissolved in MeOH (100 ml). The two solutions were then mixed rapidly and stirred at 850 rpm for 1 h at room temperature. To remove excess reagents on completion of the reaction, the solution was then subjected to four centrifuge cycles (25 min, 7,197 rcf). After each cycle, the supernatant was decanted and the remaining nanocrystals were redispersed in fresh MeOH.

Synthesis of (mPEG)ZIF-8 nanocrystals. A suspension of ZIF-8 nanoparticles (80 mg) in MeOH (8 ml) was stirred at 500 rpm with triethylamine (0.5 ml) at room temperature for 20 min. While stirring, methoxypolyethylene epoxide (mPEG; PEG average M_n = 750 g mol^{-1}; 300 mg) was added. The solution was then heated to 45 °C and stirred for 3 days. To remove unreacted mPEG, the solution was centrifuged four times (20 min, 7,197 rcf). After each cycle, the supernatant was discarded and the resulting nanocrystals were redispersed in fresh methanol. The washed nanoparticles were dried under vacuum at 45 °C for 3 h and then resuspended in water to form aqueous dispersions at different concentrations.

Synthesis of ZIF-67 nanocrystals. ZIF-67 was synthesized in MeOH following a previously reported procedure[34]. Briefly, $Co(NO_3){\cdot}6H_2O$ (1.44 g, 0.0094 mol) was dissolved in MeOH (200 ml). In a separate flask, mIm (3.24 g, 0.039 mol) was dissolved in MeOH (200 ml). The two solutions were then mixed and stirred at 800 rpm for 12 min, after which stirring was stopped and the solution was left at room temperature overnight. Nanocrystals were collected and purified by four centrifugation cycles (25 min, 7,197 rcf). After each cycle, the supernatant was decanted and the remaining nanocrystals were redispersed in fresh MeOH.

BSA/ZIF-67 functionalization. BSA with ≥98% purity was purchased from Sigma as a lyophilized powder and used as received. To use BSA to disperse ZIF-67 particles in H_2O, the protein was first dissolved in H_2O at a target concentration. Separately, dispersions of ZIF nanoparticles in MeOH were dried under vacuum. The dry ZIF powder was then added directly to the aqueous BSA solution, which was then sonicated and vortexed for 5 min at room temperature to facilitate adsorption and dispersion. Note that the protein crystal structure shown in Fig. 1d is of a BSA monomer.

Material characterization

Nanoparticle size analysis. Dynamic light scattering (DLS) and scanning electron microscopy (SEM) (Zeiss Ultra Plus) were used to quantify the particle size distribution of all synthesized nanocrystals. DLS measurements were performed using a Malvern Zetasizer Ultra, whereas SEM images were acquired using a Zeiss Ultra Plus microscope. To prepare samples for DLS, a given colloidal solution was diluted with nanopure H_2O to a final volumetric concentration of about 0.1–0.2%. Note that dilution is required to obtain accurate DLS data for samples at high concentrations. Particle dispersion and aggregation over time were monitored visually and by repeating the DLS measurement. The same conditions and instrument were used to run zeta potential measurements to characterize the surface hydrophilicity of ZSM-5 and silicalite-1. To prepare samples for SEM imaging, a given colloidal solution was diluted to a concentration near 0.1 mg ml^{-1} with EtOH and drop cast on Si wafers that had been previously cleaned by sonicating for 1 min in fresh acetone three times followed by sonicating for 1 min in fresh isopropanol three times. The SEM images were processed and analysed using MIPAR. At least 100 nanocrystals were imaged to obtain average sizes for each sample.

Concentration measurements. Nanocrystal concentrations were determined using one or more of the following techniques: ICP-AES, thermogravimetric analysis (TGA) and manual drying and weighing (Supplementary Table 3). ICP-AES measurements were performed for zeolite colloidal solutions by Galbraith Laboratories using method ME-70 after digesting samples with hydrofluoric acid. TGA measurements were performed on a TA Instruments TGA 550. Samples (20 µl) were pipetted into open Al pans with a stainless-steel bail under air and heated at a rate of 5 K min^{-1} to 600 °C under a 10 ml min^{-1} N_2 flow with an empty Al pan and stainless-steel bail used as a reference. The TGA mass was calibrated using a series of three reference masses, whereas the TGA temperature was calibrated to the Curie temperature of Ni. For zeolite samples, the mass remaining at 600 °C was taken to correspond to the mass of nanocrystals in solution. For manual drying and weighing, a known volume of aqueous dispersion (typically 50–100 µl) was pipetted into a preweighed vial, dried at 130 °C and weighed. To obtain the true mass of sample, the obtained mass of the sample was corrected for the amount of adsorbed H_2O under ambient conditions as determined from the mass loss in TGA between 25 °C and 150 °C. All ZIF colloidal solution concentrations were determined by manual drying and weighing.

Density measurements. Density measurements were performed using an Anton Paar DMA 4100 variable temperature density meter, which has an accuracy of ±0.0001 g ml^{-1}. Before each measurement, the instrument calibration was verified at 20 °C and ambient pressure. Briefly, the density of ambient lab air and the density of nanopure water were recorded and compared with the expected values. A verification was deemed successful if the density of air was 0.0012 ± 0.0002 g ml^{-1} and the density of nanopure water was 0.9982 ± 0.0002 g ml^{-1} at 20 °C. After calibration verification, the sample cell was briefly dried using a built-in air pump to prepare for sample injection. For each measurement, a sample (1.1 ml) was injected into the sample cell, with the syringe left in the injection port to prevent movement of the sample or the entry of gas bubbles. The density of the sample was recorded at 15 °C, 25 °C and 37 °C. The sample was then carefully removed using the syringe and diluted to obtain measurements at other concentrations. The sample cell was washed with at least 20 ml of nanopure water and dried with an air pump between each measurement.

Viscosity measurements. An electromagnetically spinning viscometer (EMS-1000S, Kyoto Electronics Manufacturing) was used to measure the viscosity of the high-concentration dispersions of 90-nm silicalite-1 and 193-nm ZSM-5 nanocrystals. For ZSM-5, 800 µl of aqueous solution was placed in a glass tube with a 4.7-mm diameter Al ball. During the measurement, the Al ball was set to rotate with an input frequency of 1,000 Hz. Rotation of the Al ball was traced with a red laser and the viscosity was determined by the reduction in rotational speed. Each measurement was repeated at least three times at 25 °C. The reported viscosity and shear rates are determined as the average ± the standard deviation of these trials. In cases in which the standard deviation is below the accuracy of the instrument, the standard deviation is instead replaced by the base accuracy reported by the instrument (±0.1 when the reading is above 10 mPa s or 1 s^{-1}, and ±0.01 when the reading is below 10 mPa s). Water was subsequently added to dilute the sample to a lower concentration, and the concentration of each solution was measured separately following measurement. The above procedure was repeated for 90-nm silicalite-1 dispersions, except that a 2-mm diameter Al ball was used instead, with a corresponding starting volume of 500 µl.

Solid-state gas adsorption measurements. Solid powders were obtained by drying solutions of dispersed nanocrystals overnight in an oven at 130 °C. Powders were loaded into glass sample tubes and activated under vacuum overnight at 175 °C for post-calcined silicalite-1 and ZSM-5, 100 °C for pre-calcined silicalite-1, 120 °C for ZIF-8 and ZIF-67, and 75 °C for (mPEG)ZIF-8 using a Micromeritics SmartVacPrep equipped with a turbomolecular pump. Adsorption data were then recorded using a Micromeritics MicroActive 3Flex 3500. BET surface areas and pore volumes for each material were obtained from N_2 adsorption isotherms at 77 K (Extended Data Fig. 3, Supplementary Figs. 27–31 and Supplementary Table 4). Isotherm measurements near ambient temperature were performed using a recirculating dewar connected to an isothermal bath. Note that O_2 and CO_2 isotherms at 15 °C, 25 °C and 37 °C were obtained on the same batch of material for which solution-phase adsorption measurements were performed (Extended Data Fig. 4 and Supplementary Figs. 32–36).

Gas adsorption isotherms for aqueous colloidal solutions. Adsorption measurements in solution were performed on a Micromeritics MicroActive 3Flex 3500 using a manual experimental procedure described in the Supplementary Text. We note that careful setup and analysis is required to obtain accurate gas sorption data using a volumetric instrument when the sample has a measurable vapour pressure, as the accuracy of the measurement relies solely on measurements of changes in total gas pressure. To ensure the accuracy of these measurements, control experiments for O_2 and CO_2 absorption in pure water were conducted at 25 °C (Supplementary Tables 14–16). Experimental O_2 and CO_2 absorption amounts were compared with known solubility values in pure water to obtain a % of the expected value. The standard deviation across three independent runs of the % of the expected value was used to obtain the error associated with the isotherm measurement.

Oxygen adsorption kinetics measurements. Oxygen adsorption kinetics were monitored using a PyroScience GmbH FireSting-O_2 sensor using OXSP5 fibre optic sensor spots. In brief, the sensor spot was attached to the wall of a 1.2-ml or a 4-ml vial, in which approximately 0.7–1.2 ml of nanocrystal solution was loaded. The vials were then capped with a red rubber septum with one inlet needle and one outlet needle inserted. The solution was then placed under 1 bar of flowing O_2 while stirring and allowed to equilibrate until a steady-state pO_2—indicating full equilibration—was reached.

Oxygen-release measurements in deoxygenated water. Aqueous solutions were loaded into 2-ml or 4-ml glass vials, each equipped with a Teflon stir bar and capped with a rubber septum with one inlet needle and one outlet needle inserted. Oxygenation was performed by flowing a continual stream of humidified O_2 over the sample and was continued until the pO_2 of the solution reached about 1 bar. The solution pO_2 was measured using a contact-free fibre optic probe.

Oxygen release into deoxygenated water was quantified with a Unisense MicroRespiration O_2 microsensor. Briefly, nanopure water was deoxygenated by sparging with N_2 for at least 30 min. A two-point calibration was performed on the sensor before the measurement of a specific aqueous solution. Specifically, the sensor was placed in fully nitrogenated water to obtain the mV reading corresponding to a concentration of 0 mg l^{-1}. Next, the sensor was placed in air-equilibrated nanopure water of a known temperature to calibrate the corresponding mV reading to the known mg l^{-1} (obtained from an O_2 concentration table). After calibration, an aliquot of deoxygenated water was then sealed in an air-tight 1.2-ml measurement chamber possessing two gas-tight ports and a glass stir bar. Note that the measurement chamber was completely filled with water to ensure that no headspace was present. The O_2 probe was placed inside the measurement chamber through one of the ports and a baseline concentration (mg l^{-1}) was recorded. Then, a known volume of a nanocrystal solution was injected into the sealed measurement chamber and the change in mg l^{-1} was measured to calculate the amount of O_2 released into water. The temperature of the solution in the vial was also recorded either by directly inserting a thermocouple into the vial right after the measurement or by measuring the temperature of water in an adjacent vial.

Oxygen-release measurements in packed red blood cells. To make the aqueous solutions isosmotic with blood, enough dextrose was added to afford a final concentration of 5% dextrose (w/v). The samples were then oxygenated with 1 bar of O_2 by sealing an aliquot of each solution in a 4-ml glass vial with a septa cap and piercing the cap with a needle. The vial was then placed into a three-neck round-bottom flask whose joints were connected to an O_2 inlet with a H_2O bubbler, a vacuum pump and an oil bubbler outlet. The vial was continuously stirred and three evacuation/refill cycles were performed on the sample. Specifically, the pressure was gradually decreased inside the flask over at least 15 min to 50 mmHg before continuing to evacuate at 50 mmHg for another 15 min. The total duration of evacuation was about 1 h. Following evacuation, the flask containing the samples was opened to flowing humidified O_2 for 45 min. After three evacuation/refill cycles, the sample was left under flowing O_2 overnight.

Similar to the oxygenated samples, the dispersions used for the N_2 controls were also first mixed with dextrose to afford a final concentration of 5% dextrose (w/v) before being loaded into a glass vial with a septum. To nitrogenate the solutions, each sample was first evacuated under reduced pressure (30 mmHg) for less than ten minutes. Afterwards, the sample was left under humidified, flowing nitrogen overnight to allow for full gas exchange.

Colloidal stability determination. The long-term colloidal stability of aqueous nanocrystal solutions was evaluated in one or more of the following ways: visual observation for sedimentation, DLS over time and SEM. For the visual method, a nanocrystal solution was placed in a 4-ml vial and left undisturbed over a period of time; the solution was then examined for any settling or sedimentation that may have occurred (Supplementary Fig. 48). Sixty-nanometre and 90-nm silicalite-1 dispersions showed remarkable stability even after several months. DLS measurements were also used to check for any aggregation in solution (Extended Data Fig. 8). For silicalite-1, ZSM-5, and (mPEG)ZIF-8 (Extended Data Fig. 8), multi-angle DLS was conducted immediately after synthesis and then after 1 week to compare the particle size distribution. For (mPEG)ZIF-8, the nanocrystal size distribution was also determined by SEM after 1 week and compared with that of the pristine ZIF-8 (Extended Data Fig. 8). Both approaches showed minimal changes in particle size over a period of a week, confirming the stability of the nanocrystal solutions. No settling was observed for BSA/ZIF-67 samples over 9 days in water using the same approaches outlined above for colloidal stability. PEG/ZIF-67 did show some settling over the same period, but redispersion occurred easily by gently shaking the vial with no aggregates observed by DLS.

Particle stability in water and dextrose. The stability of colloidal nanocrystal solutions was evaluated in pure water (for silicalite-1, ZSM-5, (mPEG)ZIF-8, PEG/ZIF-67 and BSA/ZIF-67) and 5% dextrose (w/v) in water (for silicalite-1, ZSM-5 and (mPEG)ZIF-8). For all samples, fresh dispersions were left undisturbed at ambient conditions for at least 1 week before further characterization. The nanocrystals were then isolated by centrifugation, and the supernatant was characterized by ICP analysis for relevant elements (Si for zeolites, Zn for (mPEG)ZIF-8 and Co for PEG/ZIF-67 and BSA/ZIF-67) to determine the degree of dissolution, if any. The precipitated nanocrystals were characterized by SEM, powder X-ray diffraction (PXRD) and gas sorption measurements. Dispersed nanocrystals were also characterized by DLS measurements soon after the dispersion was formed and again after at least 1 week.

Particle stability in blood. The stability of silicalite-1 and (mPEG)ZIF-8 in blood was evaluated by incubating the nanocrystal solutions with red blood cells for 24 h. In the case of silicalite-1, about 15 ml of packed human red blood cells were diluted with 20–25 ml of Plasma-Lyte and buffered with 300 mg of sodium bicarbonate. Three hundred and fifty microlitres of a colloidal solution of silicalite-1 nanocrystals (10.4 vol%) in 5% dextrose was subsequently added to about 6 ml of red blood cell solution. The resulting mixture was placed on a shaker and incubated at 37 °C for about 24 h. On completion, the red blood cells were lysed with 3 ml of 10% sodium dodecyl sulfate (SDS) and diluted to a total of 30 ml with H_2O. The clear red solution was centrifuged at 12,000 rpm for 10 min. The supernatant was decanted and the resulting precipitate was washed two more times with approximately 2% SDS until a light blue precipitate was obtained. The precipitate was subsequently dried and analysed by PXRD and SEM.

In the case of (mPEG)ZIF-8, 5 ml of packed human red blood cells were first washed at least five times with phosphate-buffered saline at 3,500 rpm to remove excess citrate, which can coordinate to the Zn centres of ZIF-8, that was present in the donated blood as an anticoagulant. After washing, the resulting packed red blood cells were diluted with phosphate-buffered saline. Five hundred microlitres of 5.4 vol% (mPEG)ZIF-8 was then added to 500 µl red blood cell solution and the resulting mixture was placed on a shaker and incubated at room temperature for about 24 h. On completion, the red blood cells were lysed with SDS solution as described for silicalite-1. The lysate was then frozen in liquid N_2 for transport and was subsequently thawed and washed with SDS. The product was analysed by PXRD and SEM. We note that the 24-h incubation periods were far longer than the timescale of the blood O_2 release experiments, for which nanocrystals solutions were only equilibrated in blood for 5–10 min before measuring the O_2 content by means of blood gas analysis.

All-atom MD simulations of nanoparticle gas uptake in water

Silicalite-1 simulation method. To investigate the absorption of O_2 molecules in aqueous solutions of silicalite-1 nanocrystals, we created a spherical nanocrystal (approximately 10 nm in diameter) from a silicalite-1 crystal of dimensions 16.1 nm × 15.8 nm × 15.8 nm (Fig. 3 and Supplementary Fig. 55). The particle shape is maintained through covalently bonded interactions among Si and O atoms described by the atomistic potential. We used parameters compatible with the AMBER force field to represent the bonded and non-bonded interactions of the silicalite-1 nanocrystal[47]. The resulting nanocrystal surface contains several O atoms with incomplete coordination, namely, those coordinated to only one Si atom. The surface O atoms with incomplete coordination were protonated to create silanol groups on the silica surface. The nanocrystal contains approximately 4.2 silanol groups per nm^2. The charged siloxide groups represent about 1% of the surface groups of the nanocrystal and create a surface charge density of -0.043 e nm^{-2}, equivalent to -0.7 µC cm^{-2}, in which e is the positive elementary charge. The nanocrystal was placed in a cubic box of 16.2 nm per side and solvated by water molecules. Seventeen H_3O^+ ions were added to compensate for the charge of the nanocrystal. To include a bulk gas phase, the simulation box in the *Z* direction was extended to 52 nm and O_2 molecules were inserted (Fig. 3 and Supplementary Fig. 55). At $t = 0$, the O_2 molecules are located only in the gas phase. During the simulations, the atoms of the silicalite-1 nanocrystal are unconstrained, allowing the nanocrystal to diffuse freely in the aqueous phase. We note that, by performing energy minimization and a short run of less than 1 ns, the spherical nanocrystal expands by about 10%. The nanocrystal properties are summarized in Supplementary Table 50.

We performed two simulation runs to investigate the absorption of oxygen into the silicalite-1 nanocrystal in aqueous solution. The composition for runs 1 and 2 with different initial conditions are provided in Supplementary Table 51. For run 1, the framework was solvated by randomly inserting water molecules into the simulation box, and about 3,500 water molecules were inserted randomly inside the nanoparticle before starting the run. For run 2, no water molecules were placed inside the pores of the nanocrystal at $t = 0$. We monitored the adsorption of O_2 inside the nanocrystal as a function of time until the concentration reached a stationary state.

Simulation of adsorption of O_2 by ZIF-67. Classical all-atom explicit solvent MD simulations were conducted, using the package GROMACS (version 2016.3)[48]. The force field of ZIF-67 was based on the AMBER potential for ZIF-8 (refs. [49,50]), with Zn metals in ZIF-8 replaced with Co, given the fact that ZIF-67 is isostructural to ZIF-8. The van der Waals parameters of Co in the AMBER format were used as previously reported[51]. The AMBER force field parameters of the oxygen molecule (O_2) and OH^- (counterions of ZIF-67) were obtained using the AMBER programme antechamber and converted to GROMACS format[52]. During the simulations, the (110) surface of the ZIF-67 was selected as the exposed facet in water[53]. Every second Co metal on the surface was coordinated with one −OH group, whereas the other was undercoordinated[53]. The total surface charge density is around 0.123 e nm^{-2}, which was neutralized by OH^- ions for consistency with experimental conditions. The GROMACS-formatted topology file of ZIF-67 was generated on the basis of the work of Sheveleva et al.[50].

To investigate O_2 adsorption, we created a ZIF-67 nanocrystal with dimensions of 7.2087 nm × 6.7964 nm × 6.6 nm (in the *X*, *Y* and *Z* directions, respectively), which represents 3 × 2 × 2.5 unit cells. Note that the upper and lower surfaces on the Z dimension have already been truncated when generating the (110) surfaces. Each unit cell contains two pores[50], such that there are five layers of pores along the *Z* dimension, as evidenced by the five distribution peaks of O_2 in Extended Data Fig. 7. ZIF-67 was initially located at the centre of the simulation box with dimensions of 7.2087 nm × 6.7964 nm × 48 nm (Extended Data Fig. 7). ZIF-67 was embedded in two water subphases, with a total thickness of 16 nm for water–ZIF-67–water. Six OH^- ions were included in each of the water subphases to neutralize the surface charges of ZIF-67. The water–ZIF-67–water) structure was surrounded by a gas subphase with a thickness of 32 nm. Initially, 61 O_2 molecules were included in the gas phase to replicate the combined experimental O_2 concentration inside ZIF-67 (0.107 M) and in the gas phase at 1 bar. As the simulation progressed, O_2 molecules migrated first into the water subphases and then into ZIF-67 (Supplementary Fig. 54 and Supplementary Video 3).

The energy of the system was first minimized through the steepest descent algorithm, which was followed by further equilibration under the NVT ensemble (constant number of particles, volume and temperature), which lasted 10 ps. The parameters in the equilibration simulation were similar to those in the production simulation below, except for the 1-fs integration time step used without any constraints.

In the production simulations, periodic boundary conditions were used in all dimensions. The neighbour searching was calculated up to 14 Å using the Verlet particle-based method and was updated every ten time steps. The Lennard-Jones 12-6 interactions were truncated at 14 Å (refs. [47,48]) by means of the potential-shift-Verlet method available in GROMACS. The short-range Coulomb interactions were truncated at the cut-off distance of 14 Å (refs. [49,50]) and the long-range interactions were calculated using the smooth particle mesh Ewald algorithm[54,55]. The NVT ensemble was used, and the temperatures of ZIF-67 and other molecules were separately coupled using the Nosé–Hoover algorithm (reference temperature 298 K, characteristic time 1 ps). All covalent bonds were constrained, which supported an integration time step of 2 fs. The production simulation lasted 600 ns. Calculations of the interaction energies between ZIF-67 and O_2, OH^- and H_2O (Supplementary Fig. 54) and the concentrations of O_2, OH^- and H_2O inside ZIF-67 (Supplementary Fig. 54) all supported system equilibration at 200 ns. Thus, the simulation trajectory from 200 ns to 600 ns was used to calculate the density profiles of O_2 and H_2O adsorption by ZIF-67 (Extended Data Fig. 7).

Simulation of adsorption of BSA onto ZIF-67. We performed MD simulations using the crystal structure of ZIF-67 to evaluate the adsorption of BSA onto the ZIF-67 surface. Specifically, we used a crystal of dimensions 14.4 nm × 13.6 nm × 7.3 nm, in the *X*, *Y* and *Z* directions, respectively. On the *XY* surface of the crystal, a liquid phase containing a single BSA protein, 72,000 water molecules and eight OH- ions to maintain the electroneutrality of the system were placed. The structure of BSA was used as provided in the Protein Data Bank (ID: 4F5S)[56]. The water layer thickness was approximately 11.5 nm, and the total simulation box length was 80 nm in the *Z* direction. In the *X* and *Y* directions, an infinite two-dimensional system was mimicked using the 3DC slab correction to calculate the long-range electrostatic interactions (Extended Data Fig. 7).

Data availability

The main data supporting the findings of this study are available in the paper and its Supplementary Information. Further data are available from the corresponding author on request. Source data are provided with this paper.

44. Ghorbanpour, A., Gumidyala, A., Grabow, L. C., Crossley, S. P. & Rimer, J. D. Epitaxial growth of ZSM-5@silicalite-1: a core–shell zeolite designed with passivated surface acidity. *ACS Nano* **9**, 4006–4016 (2015).
45. Tsapatsis, M., Lovallo, M., Okubo, T., Davis, M. E. & Sadakata, M. Characterization of zeolite L nanoclusters. *Chem. Mater.* **7**, 1734–1741 (1995).
46. Cravillon, J. et al. Rapid room-temperature synthesis and characterization of nanocrystals of a prototypical zeolitic imidazolate framework. *Chem. Mater.* **21**, 1410–1412 (2009).
47. Emami, F. S. et al. Force field and a surface model database for silica to simulate interfacial properties in atomic resolution. *Chem. Mater.* **26**, 2647–2658 (2014).
48. Hess, B., Kutzner, C., van der Spoel, D. & Lindahl, E. GROMACS 4: algorithms for highly efficient, load-balanced, and scalable molecular simulation. *J. Chem. Theory Comput.* **4**, 435–447 (2008).
49. Zheng, B., Sant, M., Demontis, P. & Suffritti, G. B. Force field for molecular dynamics computations in flexible ZIF-8 framework. *J. Phys. Chem. B* **116**, 933–938 (2012).
50. Sheveleva, A. M. et al. Probing gas adsorption in metal–organic framework ZIF-8 by EPR of embedded nitroxides. *J. Phys. Chem. B* **121**, 19880–19886 (2017).
51. Li, P., Roberts, B. P., Chakravorty, D. K. & Merz, K. M. Rational design of particle mesh Ewald compatible Lennard-Jones parameters for +2 metal cations in explicit solvent. *J. Chem. Theory Comput.* **9**, 2733–2748 (2013).
52. Qiao, B., Muntean, J. V., Olvera de la Cruz, M. & Ellis, R. J. Ion transport mechanisms in liquid–liquid interface. *Langmuir* **33**, 6135–6142 (2017).
53. Weng, T. & Schmidt, J. R. Structure and thermodynamic stability of zeolitic imidazolate framework surfaces. *J. Phys. Chem. B* **124**, 1458–1468 (2020).
54. Darden, T., York, D. & Pedersen, L. Particle mesh Ewald: an *N*·log(*N*) method for Ewald sums in large systems. *J. Chem. Phys.* **98**, 10089–10092 (1993).
55. Essmann, U., Perera, L. & Berkowitz, M. L. A smooth particle mesh Ewald method. *J. Chem. Phys.* **103**, 8577–8593 (1995).
56. Bujacz, A. Structures of bovine, equine and leporine serum albumin. *Acta Crystallogr. D Biol. Crystallogr.* **68**, 1278–1289 (2012).

Acknowledgements We thank A. Slavney for helpful discussions. This work was partially supported by the Arnold and Mabel Beckman Foundation through a Beckman Young Investigator grant (J.A.M.), by a DoD National Defense Science and Engineering Graduate (NDSEG) Fellowship (D.P.E.) and by a Department of Energy Computational Science Graduate Fellowship under grant DE-FG02-97ER25308 (M.B.W.). MOF synthesis and functionalization efforts were supported by the Office of Naval Research under award N00014-19-1-2148. Gas absorption and release experiments were supported under a Multidisciplinary University Research Initiative, sponsored by the Department of the Navy, Office of Naval Research, under grant N00014-20-1-2418. F.J.-A., B.Q. and M.O.d.l.C. thank the support of the Department of Energy, Office of Basic Energy Sciences under the contract DE-FG02-08ER46539 and the Sherman Fairchild Foundation. This work was performed in part at the Harvard University Center for Nanoscale Systems (CNS), a member of the National Nanotechnology Coordinated Infrastructure Network (NNCI), which is supported by the National Science Foundation under NSF award no. ECCS-2025158.

Author contributions D.P.E., M.B.W., J.C. and J.A.M. formulated the project. D.P.E., J.C., C.D., M.V.W. and R.S. synthesized the compounds. D.P.E. collected all electron microscopy images and D.P.E., J.C. and C.D. analysed all electron microscopy images. D.P.E. and M.V.W. collected the viscosity data. M.B.W. performed all density measurements. M.B.W. and J.C. collected and analysed all sorption data. D.P.E., M.B.W., J.C. and C.D. performed all oxygen-release experiments in water. D.P.E., Y.P. and B.D.P. performed all oxygen-release experiments in donated human blood. F.J.-A., B.Q. and M.O.d.l.C. designed, performed and analysed the MD simulations. D.P.E., M.B.W., J.C., C.D. and J.A.M. wrote the paper and all authors contributed to revising the paper.

Competing interests D.P.E., M.B.W., J.C., C.D. and J.A.M. are inventors on a patent application related to this work held and submitted by Harvard University.

Additional information

Supplementary information The online version contains supplementary material available at https://doi.org/10.1038/s41586-022-05029-w.

Correspondence and requests for materials should be addressed to Jarad A. Mason.

Peer review information *Nature* thanks Joaquin Silvestre Albero, Stefan Wuttke and the other, anonymous, reviewer(s) for their contribution to the peer review of this work.

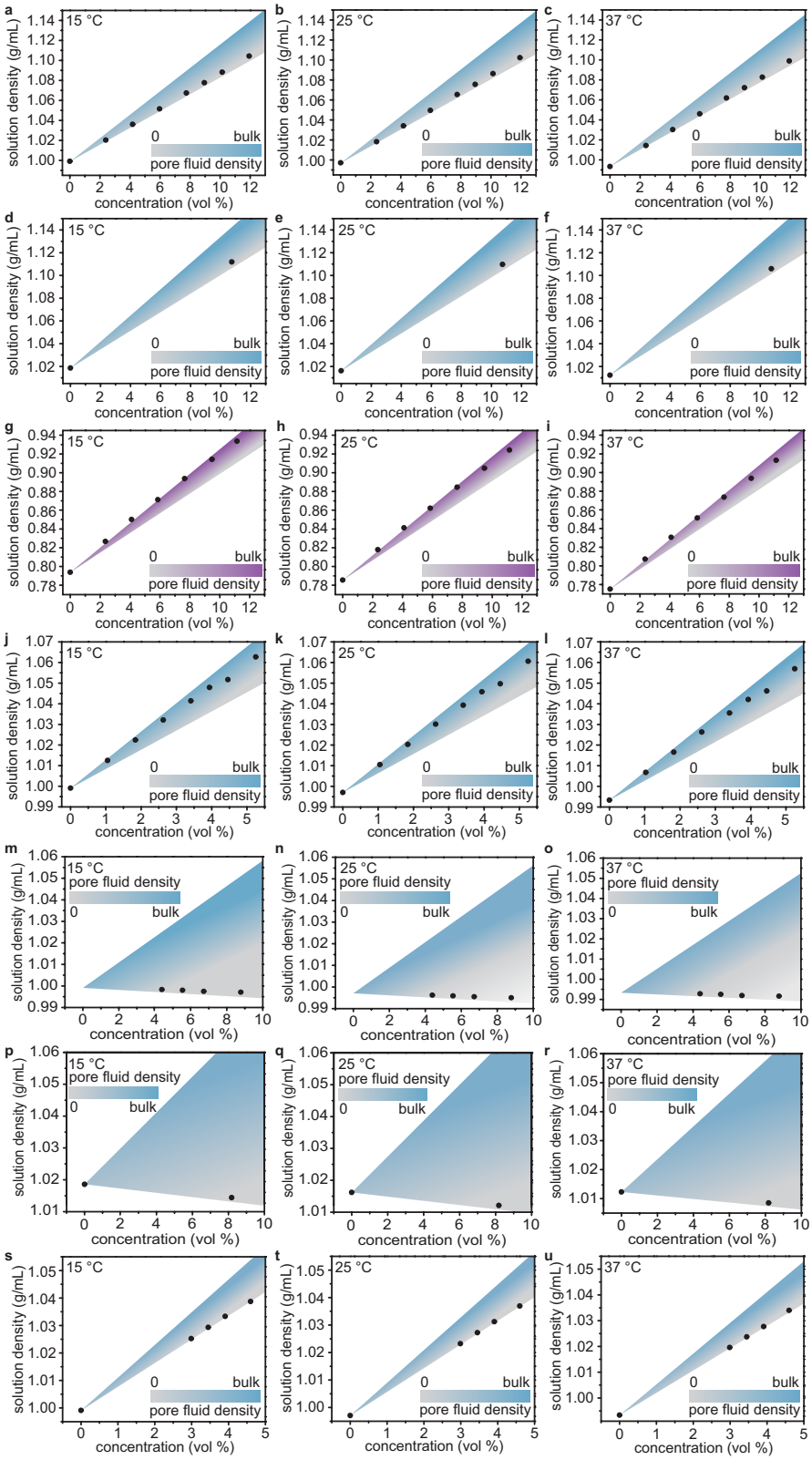

Extended Data Fig. 1 | Density measurements. Solution density (black circles) as a function of concentration and temperature for colloidal solutions of 90-nm silicalite-1 nanocrystals in water (**a**–**c**), a colloidal solution of 90-nm silicalite-1 nanocrystals with 5 wt% dextrose in water (**d**–**f**), colloidal solutions of 90-nm silicalite-1 nanocrystals in ethanol (**g**–**i**), colloidal solutions of zeolite LTL nanocrystals in water (**j**–**l**), colloidal solutions of (mPEG)ZIF-8 nanocrystals in water (**m**–**o**), a colloidal solution of (mPEG)ZIF-8 with 5 wt% dextrose in water (**p**–**r**) and colloidal solutions of ZSM-5 nanocrystals (Si/Al = 64) in water (**s**–**u**). A gradient shows the possible range of theoretical densities for different degrees of pore filling, from air-filled (grey) to solvent-filled (blue or purple) micropores. Note that the maximum pore-filling density corresponds to the bulk solvent density, but the density of nanoconfined solvent is often lower than the bulk solvent density[24].

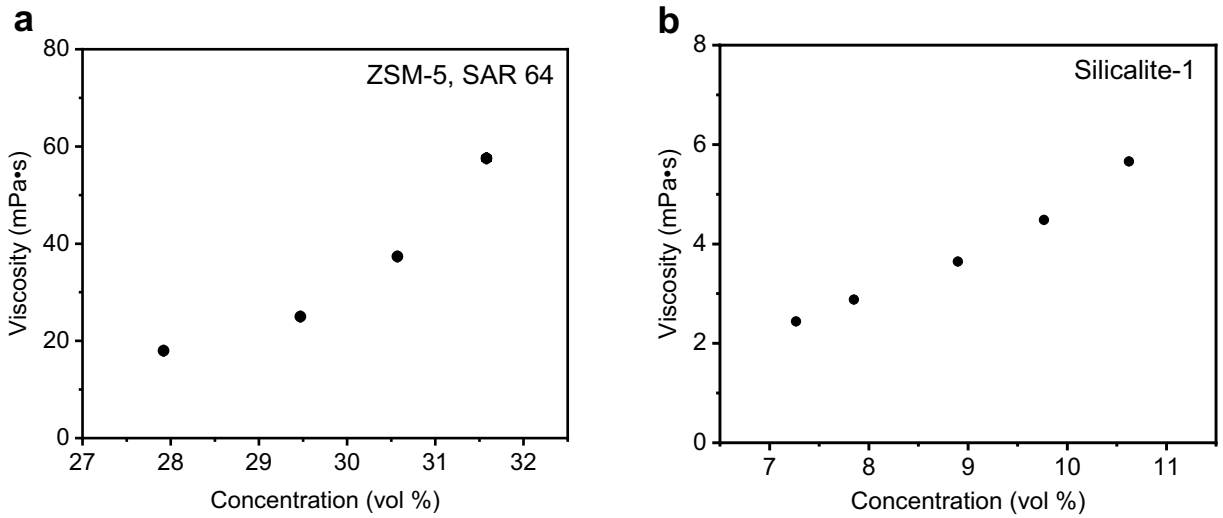

Extended Data Fig. 2 | Zeolite viscosity data. Viscosity as a function of concentration for colloidal solutions of 193-nm ZSM-5 (Si to Al / ratio, SAR = 64) nanocrystals (**a**) and 90-nm silicalite-1 nanocrystals in water (**b**) using an electromagnetically spinning viscometer at a magnetic motor rotation speed of 1,000 rpm. The measurements were taken at 25 °C.

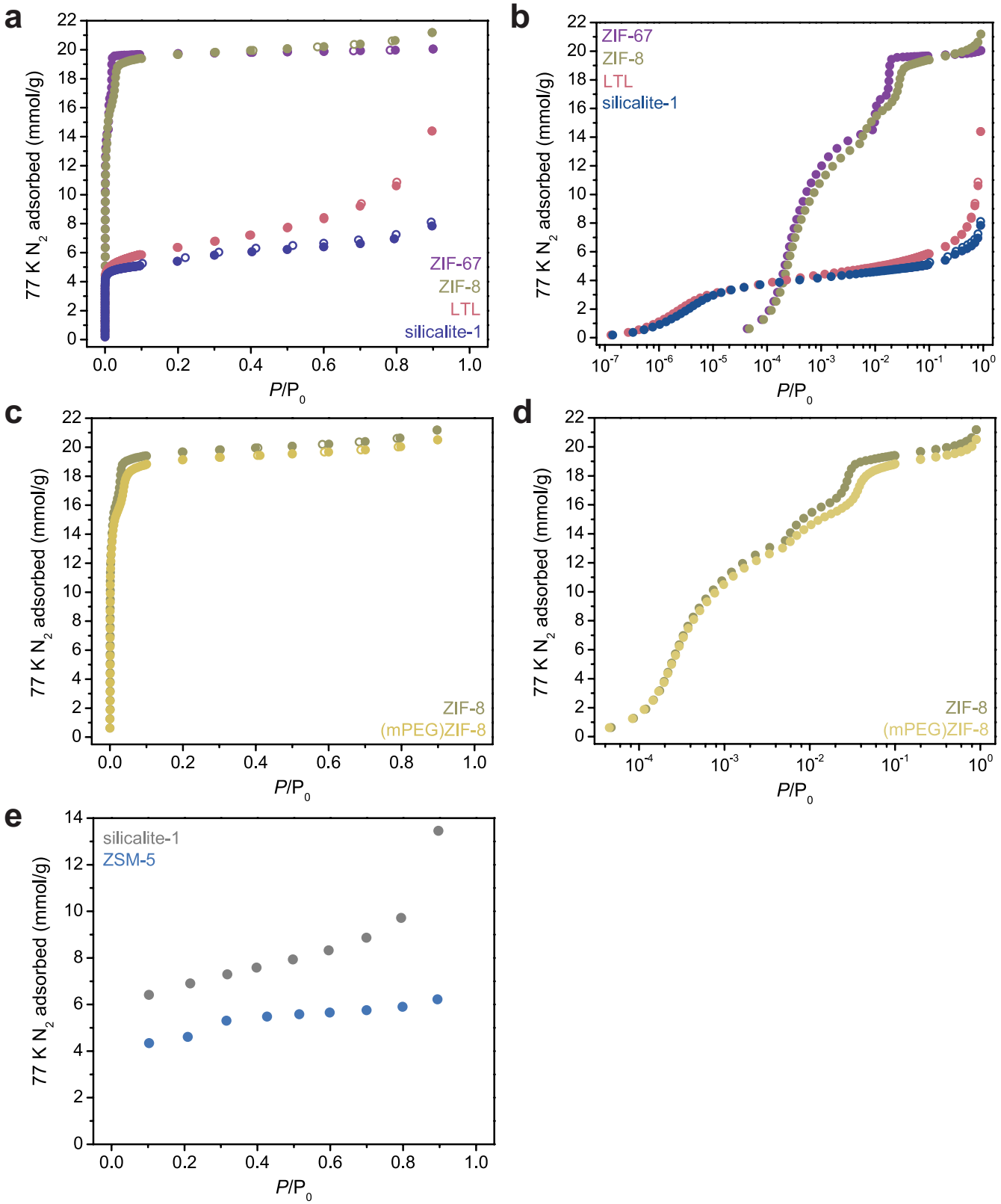

Extended Data Fig. 3 | See next page for caption.

Extended Data Fig. 3 | Surface area and pore-volume measurements. **a**, N_2 adsorption (closed circles) and desorption (open circles) isotherms at 77 K on a linear scale for as-synthesized ZIF-67, ZIF-8, zeolite LTL and silicalite-1. Calculated BET surface areas and pore volumes are listed in Supplementary Table 4. **b**, N_2 adsorption (closed circles) and desorption (open circles) isotherms at 77 K on a logarithmic scale for as-synthesized ZIF-67, ZIF-8, zeolite LTL and silicalite-1. **c**, N_2 adsorption (closed circles) and desorption (open circles) isotherms at 77 K on a linear scale for ZIF-8 nanocrystals before and after functionalization with mPEG, showing that covalent functionalization has minimal impact on the accessible surface area. **d**, N_2 adsorption (closed circles) and desorption (open circles) isotherms at 77 K on a logarithmic scale for ZIF-8 nanocrystals before and after functionalization with mPEG, showing that covalent functionalization has minimal impact on the accessible surface area. **e**, N_2 adsorption isotherms at 77 K for 60-nm silicalite-1 and ZSM-5 nanocrystals before dispersion in water. The micropore volume of 60-nm silicalite-1 calculated by the t-plot method (fit range 3.5–9.8 Å) is 0.16 ml g^{-1}, which is consistent with the micropore volume of 90-nm silicalite-1 (Supplementary Table 4). The micropore volume calculated by the t-plot method (fit range 4.7–13 Å) of ZSM-5 is 0.17 ml g^{-1}.

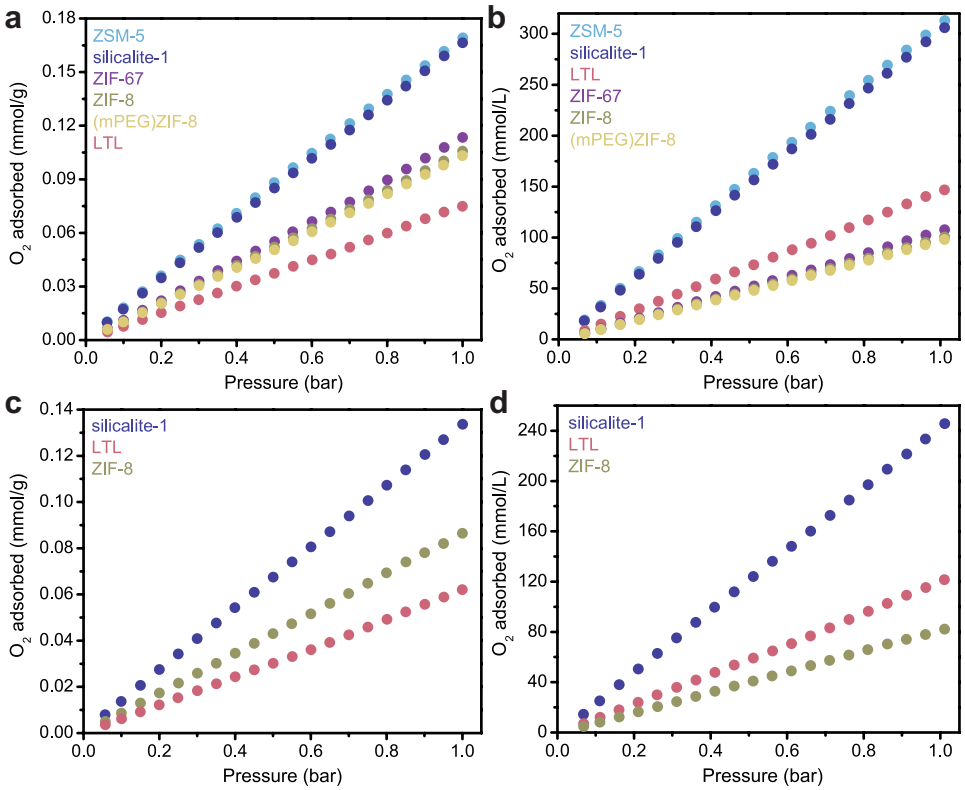

Extended Data Fig. 4 | Solid-state isotherms. O_2 adsorption isotherms at 25 °C (**a**,**b**) and 37 °C (**c**,**d**) in the solid state are plotted on a gravimetric and volumetric basis. Volumetric values are calculated from gravimetric values using the crystallographic density. Consistent with the accessible surface area, covalent functionalization of ZIF-8 has a negligible impact on adsorption of O_2, as demonstrated by comparing the isotherms for ZIF-8 and (mPEG)ZIF-8.

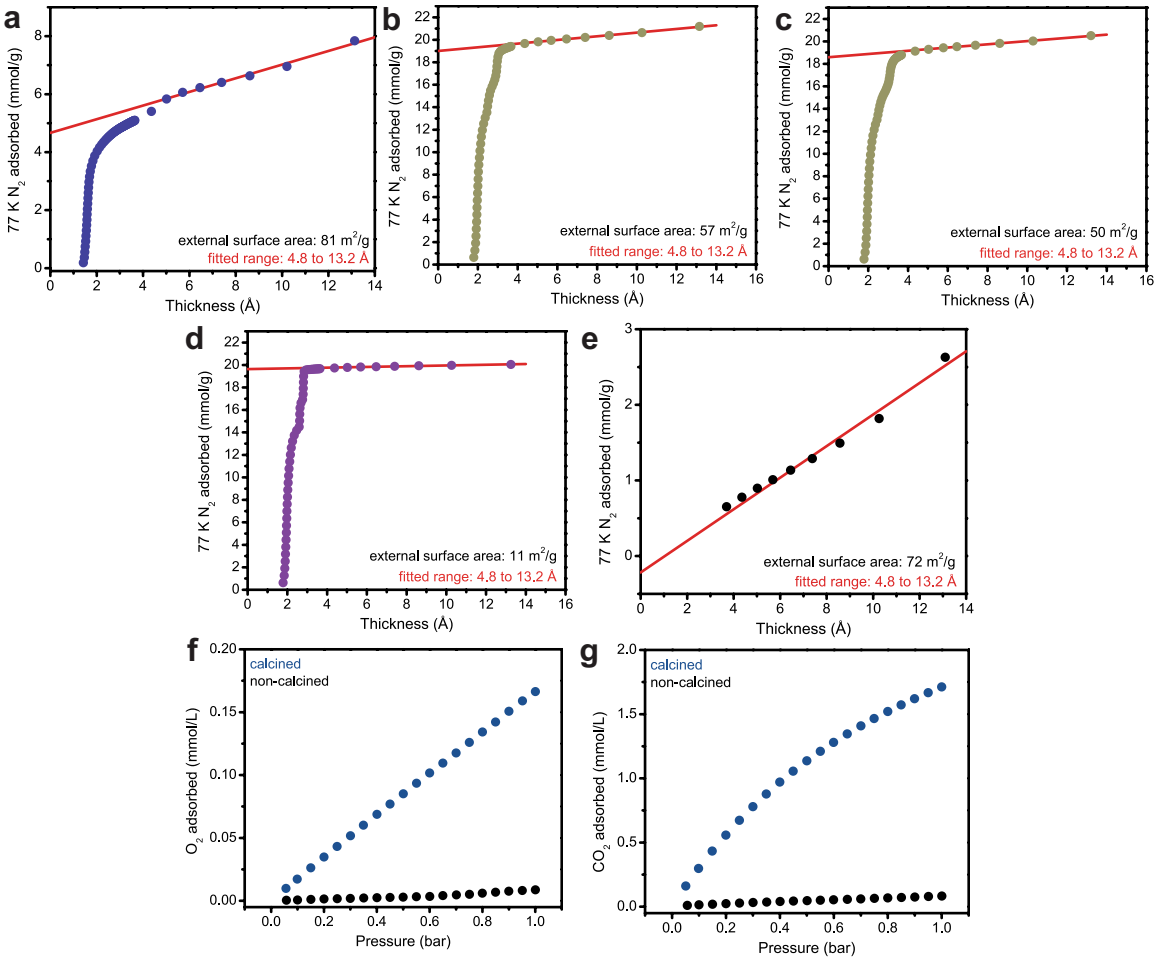

Extended Data Fig. 5 | External surface area in the solid state. Analysis of external surface area by the t-plot method using the Harkins and Jura thickness curve for 90-nm silicalite-1 nanocrystals (**a**), ZIF-8 nanocrystals (**b**), (mPEG)ZIF-8 (**c**) and ZIF-67 (**d**). Solid-state adsorption isotherms for 90-nm silicalite-1 nanocrystals before and after calcination, demonstrating the lack of accessible microporosity in non-calcined samples and the contribution of external surface area to adsorption in calcined silicalite-1. **e**, t-Plot analysis indicating that the total surface area of non-calcined silicalite-1 is consistent with the external surface area of calcined silicalite-1. Adsorption isotherms for O_2 (**f**) and CO_2 (**g**) are compared for calcined and non-calcined silicalite-1 nanocrystals at 25 °C.

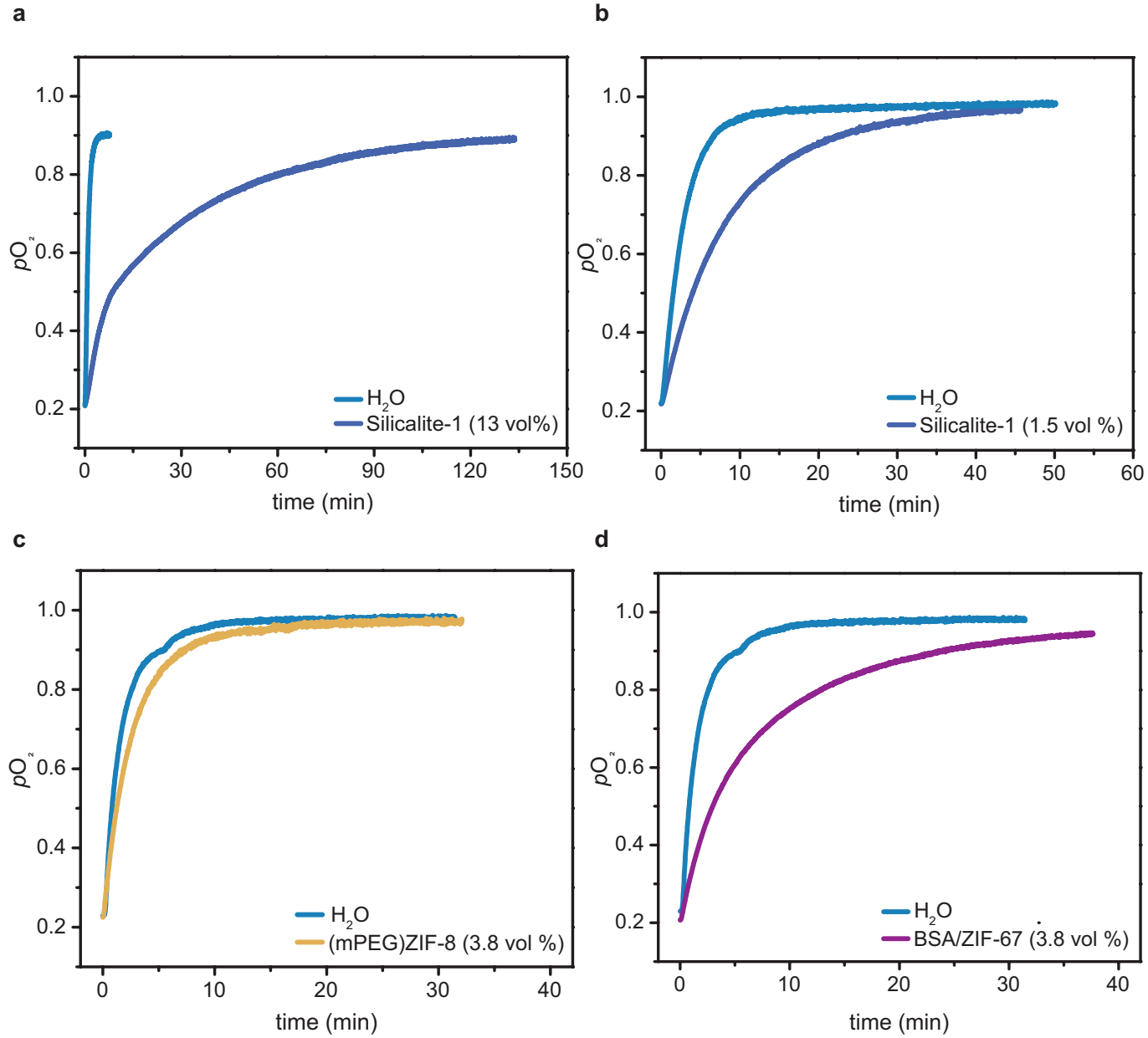

Extended Data Fig. 6 | Oxygen adsorption kinetics. Oxygen adsorption kinetics of colloidal solutions of 13 vol% silicalite-1 (navy blue) (**a**), 1.5 vol% silicalite-1 (navy blue) (**b**), 3.8 vol% (mPEG)ZIF-8 (dark yellow) (**c**) and 3.8 vol% BSA/ZIF-67 (purple) (**d**) nanocrystals in water at 20 °C are monitored under 1 bar of flowing O_2. Blank runs with pure water (blue) are included for comparison.

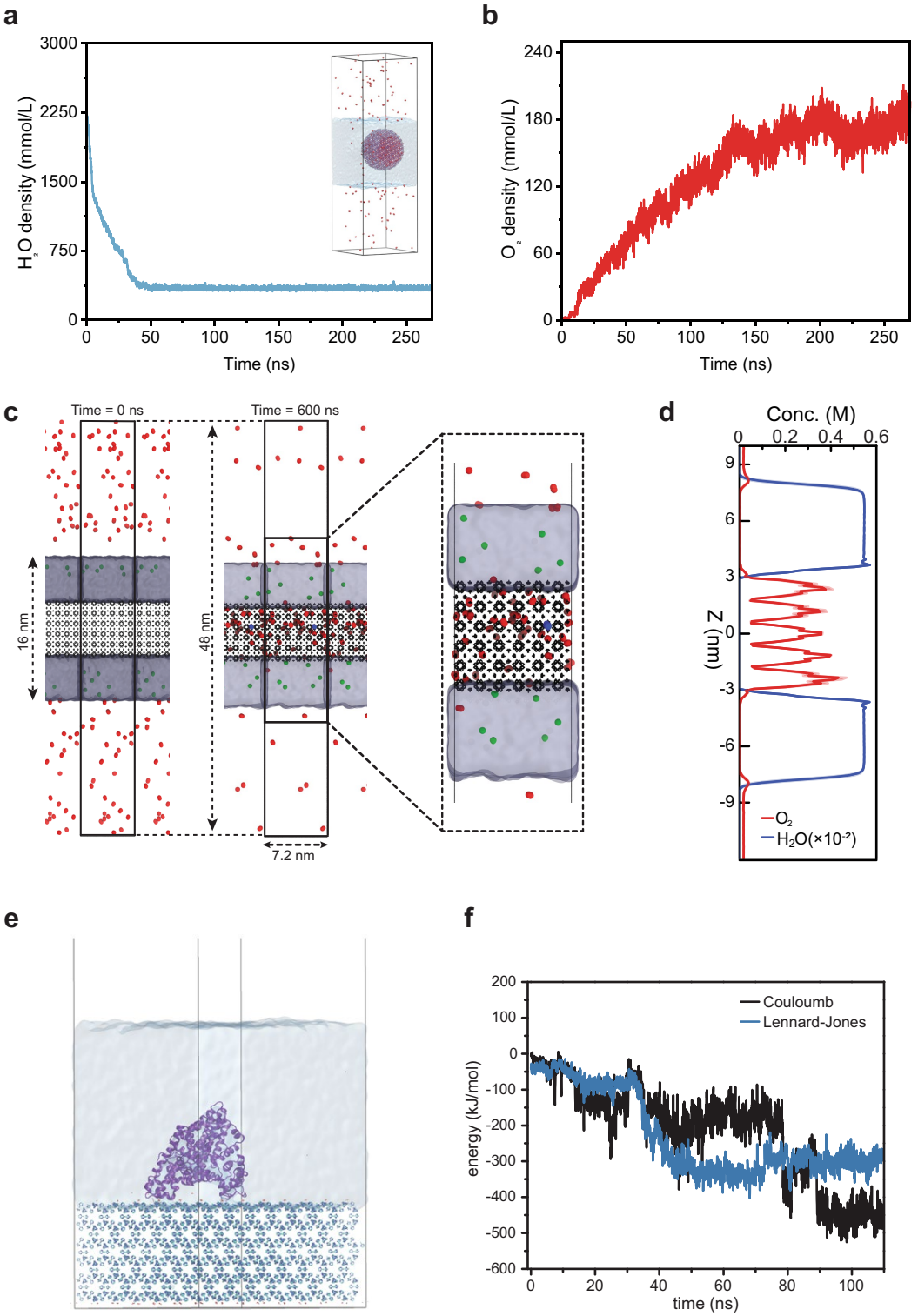

Extended Data Fig. 7 | See next page for caption.

Extended Data Fig. 7 | Silicalite-1 and ZIF-67 atomistic MD simulations. The H_2O (**a**) and O_2 (**b**) densities inside a silicalite-1 nanocrystal filled with 2,270 mmol l^{-1} H_2O molecules at $t = 0$. Note that, after addition of an initial 3,500 H_2O molecules, the system was thermalized for 1 ns before beginning the production run shown above. This initial loading of 3,500 H_2O molecules inside the nanocrystal corresponds to a starting H_2O concentration of 8,600 mmol l^{-1}. The thermodynamic driving force for water expulsion is so large that about 74% of the H_2O molecules leave before starting the production run. The residual water at the end of the simulation represents less than 2% of the total micropore volume. Atomistic simulation of O_2 adsorption inside ZIF-67 surrounded by liquid water is depicted in **c**, with snapshots of the simulation shown at 0 ns and 600 ns. ZIF-67 is coloured in black, O_2 in red and OH^- in green. ZIF-67 hydrogen atoms are omitted for clarity. The simulation box is indicated by solid black lines. The equilibrium concentration profiles of O_2 and water are shown in **d**, with the shadows representing the standard deviations from four blocks of 100-ns simulations. The relative densities in the gas phase, in the water phase and inside ZIF-67 support that the adsorption of water molecules by ZIF-67 is energetically unfavoured, whereas O_2 adsorption is favoured. A simulation of the protein BSA adsorbing on the surface of ZIF-67 is illustrated in **e**. Water is represented as a semi-transparent volume in light blue. **f**, Calculation of the interaction energy between the protein and ZIF-67. The Coulomb and Lennard-Jones components of the interaction between ZIF-67 and BSA show that the Coulomb interactions dominate.

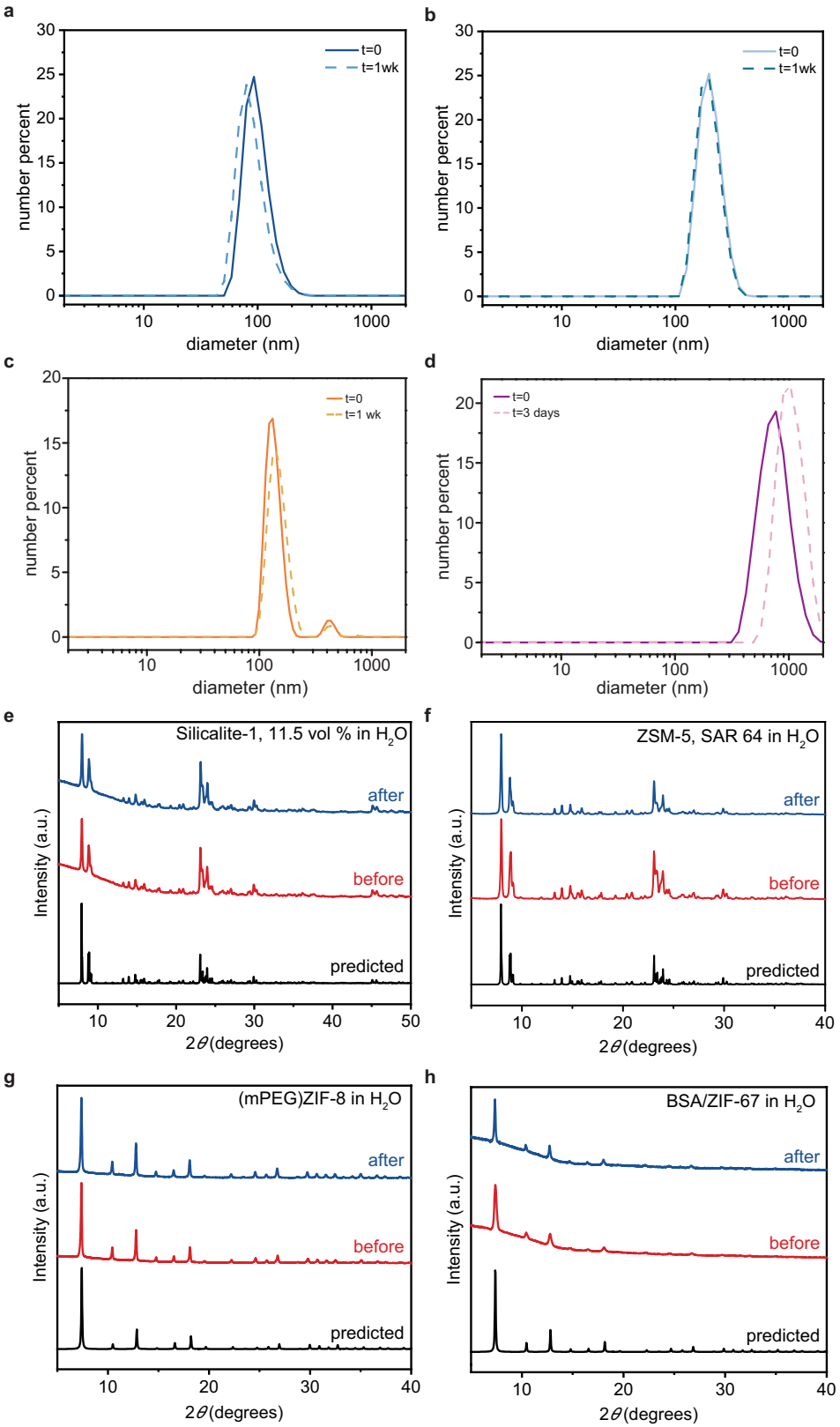

Extended Data Fig. 8 | Colloidal stability. DLS measurements of colloidal solutions of silicalite-1 (**a**), ZSM-5 (**b**), (mPEG)ZIF-8 (**c**) and BSA/ZIF-67 (**d**) nanocrystals in water before and after 1 week of stability testing. The starting solutions contained 11.5 vol% silicalite-1, 34.4 vol% ZSM-5, 8.3 vol% (mPEG)ZIF-8 and 3.4 vol% BSA/ZIF-67. The samples were diluted 70-fold (for silicalite-1), 230-fold (for ZSM-5) and tenfold (for (mPEG)ZIF-8) to obtain accurate DLS data. PXRD patterns before and after dispersion in H_2O are shown for 98-nm silicalite-1 nanocrystals (11.5 vol%) (**e**), ZSM-5 (34.4 vol%) (**f**), (mPEG) ZIF-8 nanocrystals (8.3 vol%) (**g**) and BSA/ZIF-67 (3.4 vol%) (**h**). All samples were dispersed for 1 week before PXRD characterization apart from (mPEG)ZIF-8, which was taken after 2 weeks of dispersion.

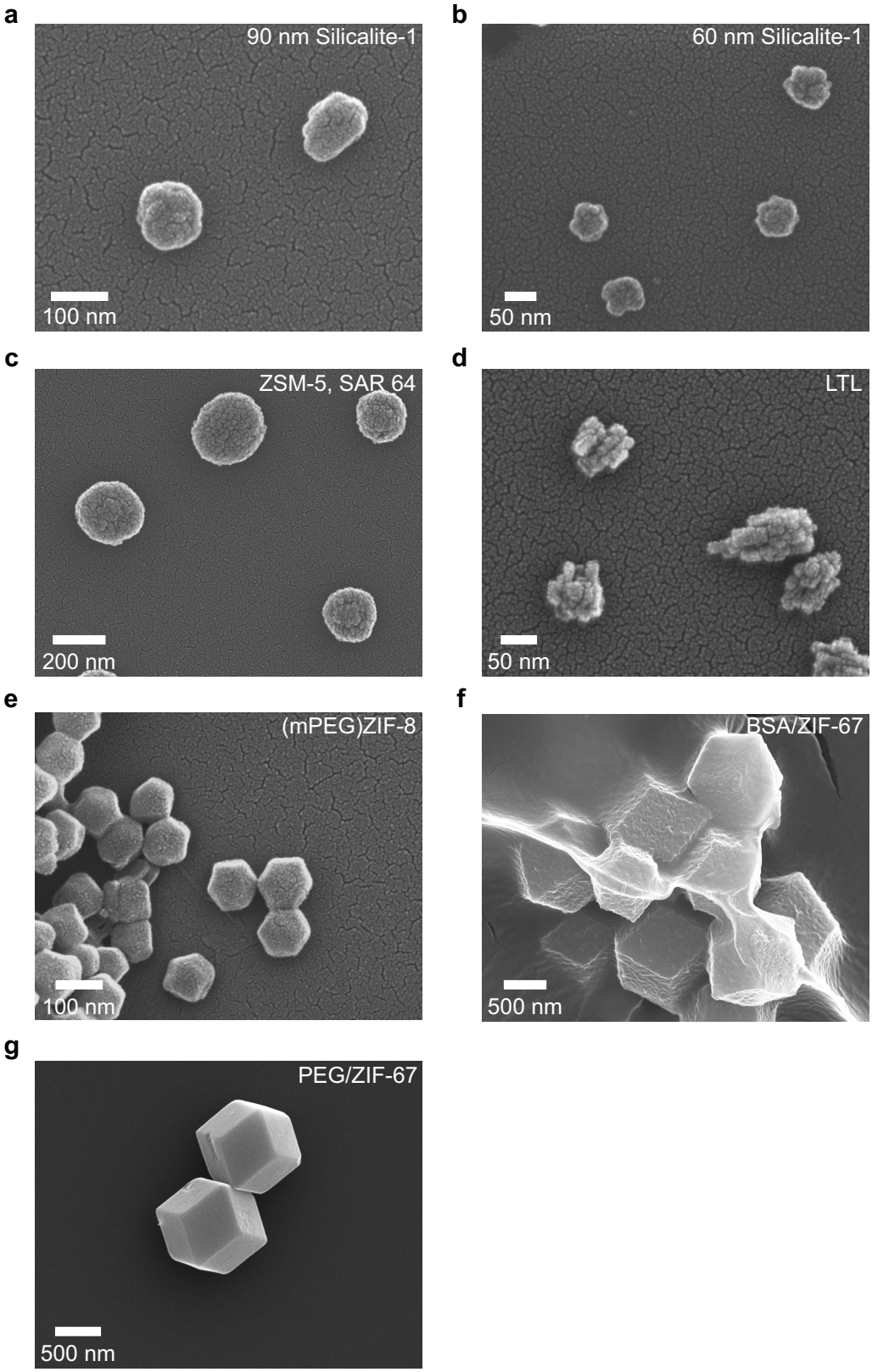

Extended Data Fig. 9 | SEM images. Representative SEM images of nanocrystals used to form colloidal solutions in water: silicalite-1 (average diameter = 90 ± 16 nm) (**a**), silicalite-1 (average diameter = 59 ± 8 nm) (**b**), ZSM-5 (average diameter = 193 ± 32 nm) (**c**), zeolite LTL (**d**), (mPEG)ZIF-8 nanocrystals (average diameter = 113 ± 10 nm) (**e**), BSA/ZIF-67 nanocrystals (average diameter = 1,010 ± 185 nm) (**f**) and PEG/ZIF-67 (**g**). All samples were sputter coated with a 10-nm layer of 80:20 Pt:Pd except for **b** and **d**, which were sputter coated with a 5-nm layer.

Extended Data Table 1 | Summary of O_2-carrying capacities

Material	O_2 carrying capacity (mL/dL)	% of theoretical capacity
Fluosol (20 vol %)[a]	5.9	
Oxygent (60 vol %)[a]	16.0	
Blood[b]	23.8	
ZSM-5 (39 vol %)	187 ± 18	72.9 ± 3.5
silicalite-1 (12.7 vol %)	89.2 ± 9.6	85.6 ± 6.5
silicalite-1 (4.0 vol %)	31.3 ± 0.1	102.4 ± 1.7
(mPEG)ZIF-8 (6.6 vol %)	18.8 ± 1.3	95.7 ± 7.4
BSA/ZIF-67 (3.6 vol %)	9.8 ± 0.9	80.4 ± 8.5
LTL (5.6 vol %)	2.8 ± 0.2	-2.1 ± 1.2
PEG/ZIF-67 (3.6 vol %)	0.7 ± 0.1	10.6 ± 3.7
PEG/ZIF-8 (3.6 vol %)	0.6 ± 0.0	6.6 ± 2.9

Amount of O_2 stored in nanocrystal solutions determined by measurement of the amount of O_2 released on injection of an oxygenated solution into deoxygenated water, along with the percentage of the experimental amount of O_2 released relative to the theoretical amount for a microporous solution based on solid-state O_2 adsorption data. At least three measurements were made for each material to obtain an average value and standard deviation. Note that all solutions were equilibrated near 1 bar of O_2 at ambient temperature, except for PEG/ZIF-8 and PEG/ZIF-67, which were equilibrated with air (0.2 bar O_2). [a]Capacities for perfluorocarbon emulsions are from ref. [36]. [b]Assuming 15 g Hb dl^{-1}.